International Journal of Solids and Structures 276 (2023) 112324

Contents lists available at ScienceDirect

International Journal of Solids and Structures

journal homepage: www.elsevier.com/locate/ijsolstr

Enhancing elongation and trading off strength versus ductility of commercially pure titanium sheets using cyclic bending under tension and annealing

Nikolai Matukhno, Nemanja Kljestan, Marko Knezevic *

Department of Mechanical Engineering, University of New Hampshire, Durham, NH 03824, USA

ARTICLE INFO

Keywords:
Strength
Elongation
Cyclic-bending-under-tension
Microstructures
Commercially purity titanium

ABSTRACT

This paper describes results acquired in an investigation into determining the influence of cyclic-bending-under-tension (CBT) and annealing on improving elongation-to-fracture (ETF) and optimizing strength and ductility of commercially pure titanium (cp-Ti) sheets. The space of process parameter involving crosshead velocity and bending depth along with sheet thickness was explored to establish a set of optimal parameters providing the greatest ETF for cp-Ti. Enhancements in ETF of about 3× were achieved using CBT relative to simple tension. Given the uniform elongation facilitated by CBT to very large strains, tradeoffs in strength and ductility of the material were examined by subjecting a set of sheets to a certain number of CBT cycles under the optimized parameters and annealing. In doing so, strength of the material increased by a factor of 1.6 along the sheet softest direction, while by a factor of 1.3 along the sheet strongest direction reducing the anisotropy. Microstructural evolution was characterized using electron-backscattered diffraction, while texture evolution was measured using neutron diffraction. These results revealed slip dominated deformation with minor activity of twinning. The role of CBT in preserving integrity of the sheets to large plastic strains is discussed by comparing measured and simulated geometries and mechanical fields.

1. Introduction

Sheet metals undergo forming into complex shapes, and then the formed parts need to provide the necessary structural properties in their final state (Barrett and Knezevic, 2019; Hosford and Caddell, 2011; Knezevic et al., 2016; Sharma et al., 2022). Much attention has focused on understanding the relationships between microstructure and response of metals, in terms of strength, work hardening rate and formability to facilitate sufficient elongation and properties of the formed parts. Achieving strength versus ductility compromises of metallic sheets typically involves expensive alloying and long heat treatment steps that are both costly. However, recent innovations in sheet metal forming can provide an alternative strategy where the elongation-to-fracture (ETF) of the sheet undergoing forming is extended using novel, but not fully understood forming operations. One such process is cyclic-bending-under-tension (CBT), which delays localized necking and subsequent failure to significantly larger strains than are generally achievable in simple tension (ST) (Benedyk et al., 1971; Emmens and van den Boogaard, 2009a). The process can also induce microstructural evolution for the purpose of targeting a specific final microstructure, e.g. increase strength (Knezevic et al., 2019) or R-value (Zecevic and Knezevic, 2023). Such an approach is particularly desirable for hexagonal close-packed (HCP) materials, such as Ti and Mg alloys, which have many desirable intrinsic properties (e.g. lightweight, biocompatible) (Staiger et al., 2006). In particular, these metals are receiving increasing interest for structural components, because of their high strength-to-weight ratio. However, HCP metals exhibit poor formability at room temperature, which is associated with difficulties in activating a sufficient number of slip systems on multiple crystallographic planes and directions (basal, prismatic, and pyramidal slip modes) and the associated need for profuse twinning for accommodating an arbitrary state of plastic strain (Manopulo et al., 2018; Risse et al., 2017; Wang et al., 2020; Wang et al., 2021; Zecevic et al., 2018; Zhai et al., 2016).

The CBT process improves ETF by slowing down damage-nucleating dislocation accumulation owing to the incremental forming nature of the process (Zecevic and Knezevic, 2023) and repeated strain reversals along with underlying loading/unloading relaxations (Varma et al.,

* Corresponding author.
E-mail address: marko.knezevic@unh.edu (M. Knezevic).

https://doi.org/10.1016/j.ijsolstr.2023.112324
Received 1 January 2023; Received in revised form 26 March 2023; Accepted 11 May 2023

Table 1
Chemical composition of cp-Ti grade 4 (wt.%) per sheet thickness.

	C	Fe	H	N	O	Ti
1 mm thickness	0.005	0.19	0.0006	0.004	0.25	Balance
1.3 mm thickness	0.009	0.16	0.001	0.009	0.35	Balance
2 mm thickness	0.005	0.19	0.0006	0.004	0.27	Balance

2018) taking place during the process. It is a well-established fact that in incremental sheet forming (ISF), levels of plastic deformation can be imparted well above the conventional forming limit curves (FLCs). Several processing mechanisms have been identified to potentially contribute to such improved formability: shear stress, normal stress (in the thickness direction), bending, and cyclic straining along with local relaxations (Emmens and van den Boogaard, 2009b). For example, Eyckens et al. carried out a detailed theoretical analysis on the effect of shear in sheet shaping, and concluded that the shear can indeed increase the stretchability (Eyckens et al., 2009). Allwood et al. conducted some similar works and included thickness stress in the analysis; they observed that the thickness stress can also raise the stretchability (Allwood and Shouler, 2009). Yagami et al. carried out tests involving cyclic straining, albeit with superimposed bending, and also found that these processes can boost stretchability (Yagami et al., 2009). That bending solely can improve stretchability has been known for long time, but it has gained recent renewed interest by observations that promise tailoring or amplification of the effect (Benedyk et al., 1971; Swift, 1948; Tamimi et al., 2020). Stretchability of sheets undergoing bending can be influenced by selecting tool radius and/or sheet thickness (Schleich et al., 2009). Moreover, the beneficial effect of superimposing bending on ST to enhance stretchability has been observed in sheet metal

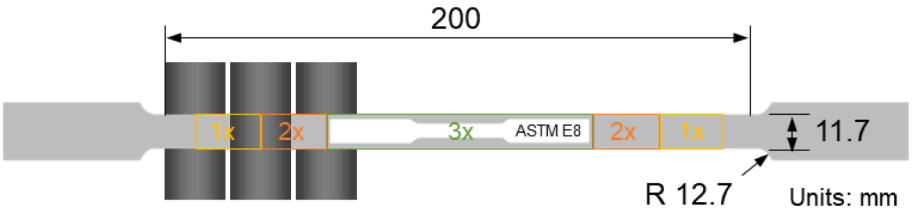

Fig. 1. A CBT specimen with 1×, 2×, and 3× deformation regions and a sub-size specimen of 32 mm gauge length and 6 mm width from the 3× region.

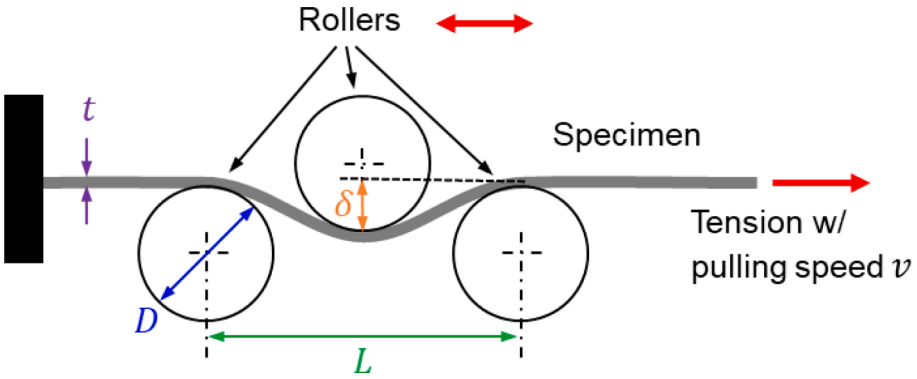

Fig. 2. Cyclic-bending-under-tension (CBT) process with bending depth (δ) adjusted using the top roller moving up and down and pulling speed as the main process parameters. The distance L between the bottom rollers is 54 mm, while the diameter D of the three rollers is 25.4 mm.

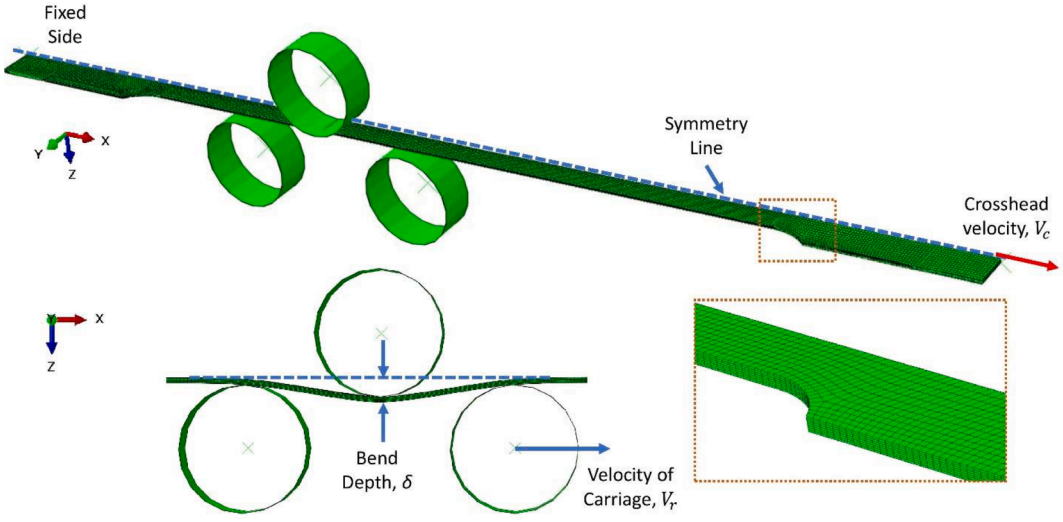

Fig. 3. FE mesh for one half of the specimen consisting of 27,590 C3D8R elements (7 elements in thickness and 9 elements in half width) along with boundary conditions created in Abaqus for simulating CBT. × = RD, y = TD, and z = ND.

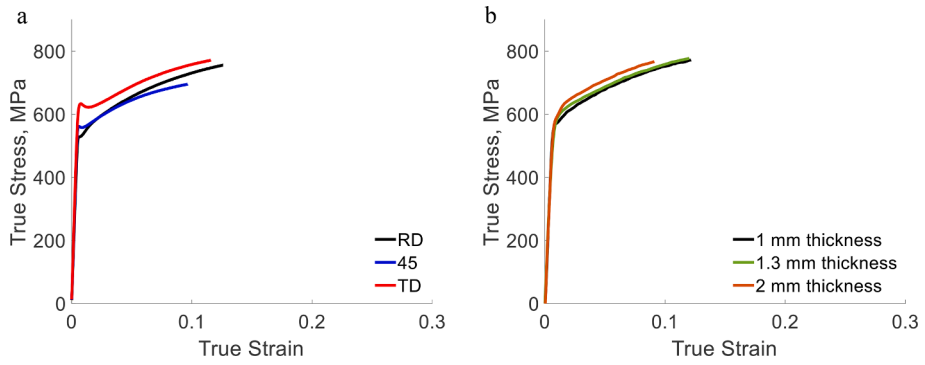

Fig. 4. (a) Measured true stress–strain curves for as-received 1 mm sheets of cp-Ti along the RD, TD, and 45° during ST under 0.001/s strain rate at room temperature. (b) Flow stress curves for as-received 1 mm, 1.3 mm, and 2 mm thick sheets of cp-Ti measured along the RD during ST under 0.001/s strain rate at room temperature.

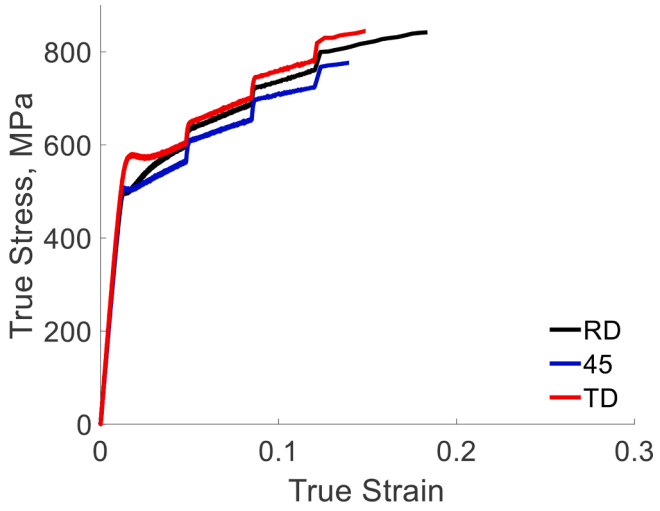

Fig. 5. Measured true stress–strain curves for as-received 1 mm sheets of cp-Ti along the three directions during ST under jumps in strain rate from 0.0001/s to 0.001/s (m_1), then from 0.001/s to 0.01/s (m_2), and finally from 0.01/s to 0.1/s (m_3).

Table 2
SRS coefficients measured for as-received 1 mm sheets of cp-Ti (grade 4) along the three directions.

Direction	m_1	m_2	m_3	Mean
RD	0.0240	0.0204	0.0217	0.0220
45°	0.0299	0.0253	0.0215	0.0256
TD	0.0314	0.0262	0.0211	0.0261

forming involving draw-beads (Nine et al., 1979). Conversely, enhanced stretchability of steels can arise from intermittent relaxations (Daroju et al., 2022b; Hariharan et al., 2013; Zecevic et al., 2016b), which is attributed to reconfiguration of dislocations into a low energy configuration (Daroju et al., 2022a; Varma et al., 2018). The rearrangement/recombination causes the internal stresses to relax (Ferreri et al., 2022; Hariharan et al., 2016; Zecevic and Knezevic, 2018). Such relaxation due to the repeated loading–unloading in CBT facilitated the development of low energy cellular dislocation substructures in an Al alloy (Knezevic et al., 2019) and dislocation tangles in a dual-phase steel (Yaddanapudi et al., 2021), which were not observed in ST.

The potential for improvements in manufacturing processes for sheet metals led to the development of an adaptable CBT test rig for deeper analysis of the effects and mechanisms, as will be shown shortly. A sheet or a strip of a metal is passed back and forth through a set of stationary rollers in the rig that impart a local bending to the sheet, while simultaneously pulled in tension under a constant velocity. While the local force-to-displacement increment is increasing in successive bending cycles, necking is avoided because ductility is incrementally depleted throughout the gauge length as opposed to localized necking at a single location in a tensile test followed by fracture. Excessive plastic deformation and hardening take place under ST in the localized neck regions followed by ultimate fracture, while the sheet outside the necked region has ample of idle remaining ductility. The CBT process is conceived to exploit such idle ductility by delaying necking (Emmens and van den Boogaard, 2009a). The best improvements in ETF using CBT were obtained from alloys that exhibit large necking in ST such as steels (Poulin et al., 2020b) and Al alloys (Roemer et al., 2019). In contrast, moderate improvements were observed for alloys failing with small necks such as AZ31 (Matukhno et al., 2022). Similarly, sheet metals with lower hardening rates show higher integrity under CBT (Emmens and Boogaard, 2011; Matukhno et al., 2022). Given that sheets can be stretched to greater strain levels using CBT than ST, the CBT test enables inferring the post-necking hardening behavior of sheets (Emmens and van den Boogaard, 2012) circumventing more involved tests (Coppieters and Kuwabara, 2014) like bulge tests (Barlat et al., 2002). The approach to infer the post-necking hardening using CBT assumes that the stress state in the sheet under CBT closely resembles that in ST (Barrett and Knezevic, 2020; Poulin et al., 2020a). The present work is concerned with characterizing the CBT behavior of commercially pure (cp) α-titanium (Ti) exhibiting substantial necking and moderate level of hardening.

Cp-Ti is widely used in different structural applications such as chemical plants, heat exchangers, and aerospace components, like leading-edge skins, because of ease of fabrication and excellent corrosion resistance, in addition to its relatively high strength to weight ratio (Boyer, 1996). Cp-Ti sheets also exhibit deformation behavior with some anisotropy and have modest ductility at room temperature; in some cases the sheets can be formed at room temperature by press forming and bending, while in others high-temperatures are required to achieve the desired part shape (i.e. via superplastic forming) (Filice et al., 2010; Zhu et al., 2005). Like many metals with a low symmetry HCP crystal structure, the mechanical response of cp-Ti is driven by the formation and growth of two defect-driven mechanisms, crystallographic slip and twinning (Hama et al., 2015; Sinha and Gurao, 2017). Such multiplicity of intrinsic deformation mechanisms in combination with pronounced texture renders the mechanical response of cp-Ti anisotropic (Baral et al., 2018), and also more strain rate and temperature sensitive than metals with cubic crystal structures (Becker and Pantleon, 2013; Peng et al., 2013; Tsao et al., 2012).

The experimental investigation presented here begun by exploring the space of process parameter involving three sheet thicknesses, several crosshead velocities, and several bending depths to establish a set of optimal parameters providing the greatest ETF for cp-Ti. Given the

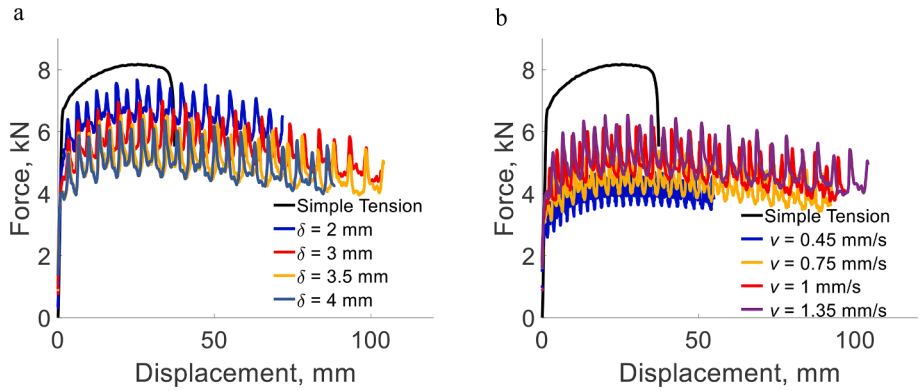

Fig. 6. Effect of process parameters on measured force–displacement curves of 1 mm cp-Ti (grade 4) sheets during CBT along the RD: (a) constant pull speed (v = of 1.3 mm/s) and (b) constant bend depth (δ = 3.5 mm). Measured force–displacement curve of the material in ST is shown for reference in both plots.

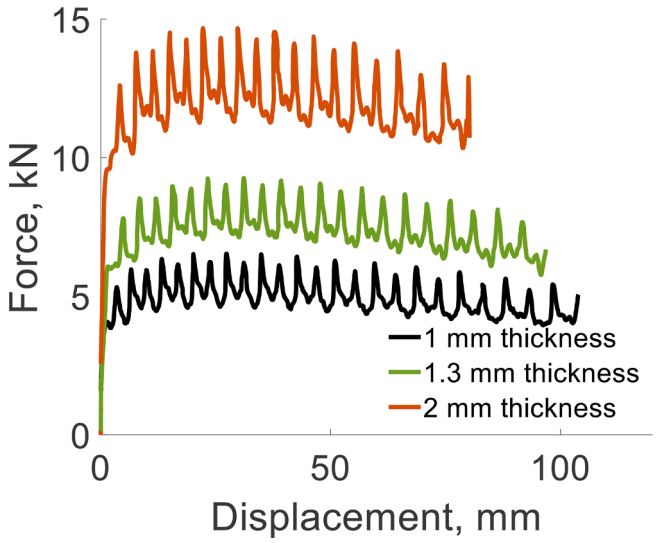

Fig. 7. Comparison of measured force–displacement curves for 1 mm, 1.3 mm, and 2 mm thicknesses cp-Ti (grade 4) sheets during CBT along the RD under 3.5 mm bend depth and 1.35 mm/s pull speed parameters.

uniform elongation facilitated by CBT to very large strains, tradeoffs in strength and ductility of the material were examined next by subjecting a set of specimens to a certain number of CBT cycles under the optimized parameters and subsequent annealing. The evolution of grain structure during CBT and annealing was observed using electron-backscattered diffraction (EBSD), while the evolution of texture was characterized using neutron diffraction (NeD). These characterization results were used to discuss microstructural changes and deformation mechanisms accommodating the plastic strains during CBT and ST of cp-Ti. Furthermore, a finite element (FE) model of the process was created in Abaqus software and used to simulate the process while predicting the load–displacement data and mechanical fields. To facilitate the simulation of the CBT process, a flow stress curve for cp-Ti needed to be extrapolated. The good predictions of the succession of spikes and plateaus inherent to the CBT load–displacement curve validated the extrapolated flow stress curve. The profiles of axial stress and triaxiality were probed through the sheet thickness to discuss the stabilizing mechanisms of the CBT process preserving integrity of the sheets to large plastic strains in function of sheet thickness. Moreover, measured strain fields using digital image correlation (DIC) were compared with the predictions to elucidate the location and onset of failure axially. Comprehensive data in terms of improving ETF with CBT and enhancing the strength while preserving some residual ductility with CBT and annealing of cp-Ti along with simulations results providing insights in the kinematics of the process are presented and discussed in this paper.

2. Material, experimental and simulation procedures

This section explains the studied material, experimental procedures for testing, heat treating (HT), microstructural characterization, and a simulation setup for the CBT test.

2.1. Material

1 mm, 1.3 mm and 2 mm sheets of cp-Ti were obtained from Fine Metals Corporation under a specification: AMS-T-9046 CP-1 (grade 4). The material was received in an annealed condition. Table 1 shows the composition per sheet thickness.

2.2. Mechanical testing

ST monotonic tests were performed first at a nominal strain rate of 10^{-3} s^{-1} and room temperature (RT) to breaking along three sheet direction, the rolling direction (RD), diagonal direction (45°), and transverse direction (TD). Next, strain rate sensitivity (SRS) jump tests were performed along the same three direction. The SRS jumps from 0.0001/s to 0.001/s for m_1 from 0.001/s to 0.01/s for m_2, and from 0.01/s to 0.1/s for m_3 were performed at RT to breaking. The SRS coefficients were calculated using $m = \ln\frac{\sigma_2}{\sigma_1}/\ln\frac{\dot{\varepsilon}_2}{\dot{\varepsilon}_1}$ where 1 and 2 represent strain rate before and after a given jump, i. These tests were performed using specimens having a gauge length 50 mm and width 12.5 mm on an MTS Landmark 370 servo hydraulic mechanical testing machine. An MTS extensometer 632.12F-20 was used to measure displacement, which was verified with the displacement of the actuator.

CBT testing/processing was performed using specimens with geometry shown in Fig. 1. The specimen geometry is a suitably modified ASTM E8 specimen such that the rollers always travers the gauge of sufficient length. The deformation regions are defined based on the number of sheet bandings are indicated in the figure as 1×, 2×, and 3×. Last type of test specimens used in the study are sub-size specimens used for secondary ST testing of CBT processed strips, as shown in Fig. 2. The sub-size specimens had a gauge length 32 mm and width 6 mm based on ASTM E8 (2015). The sub-size specimens were cut by water jet as slightly oversized and then machined by a 3-axis CNC machine to the specified geometry. The secondary testing was used to evaluate strength and residual ductility after CBT and annealing processing.

A CBT machine recently built at the University of New Hampshire (UNH) is shown in the appendix. A schematic of the process is shown in Fig. 2. The machine differs from other ones used in prior literature (Benedyk et al., 1971; Tamimi et al., 2020) because the three rollers are stationary (but free to rotate) and the material undergoing CBT flows through them. Also, the machine is designed for processing of wide

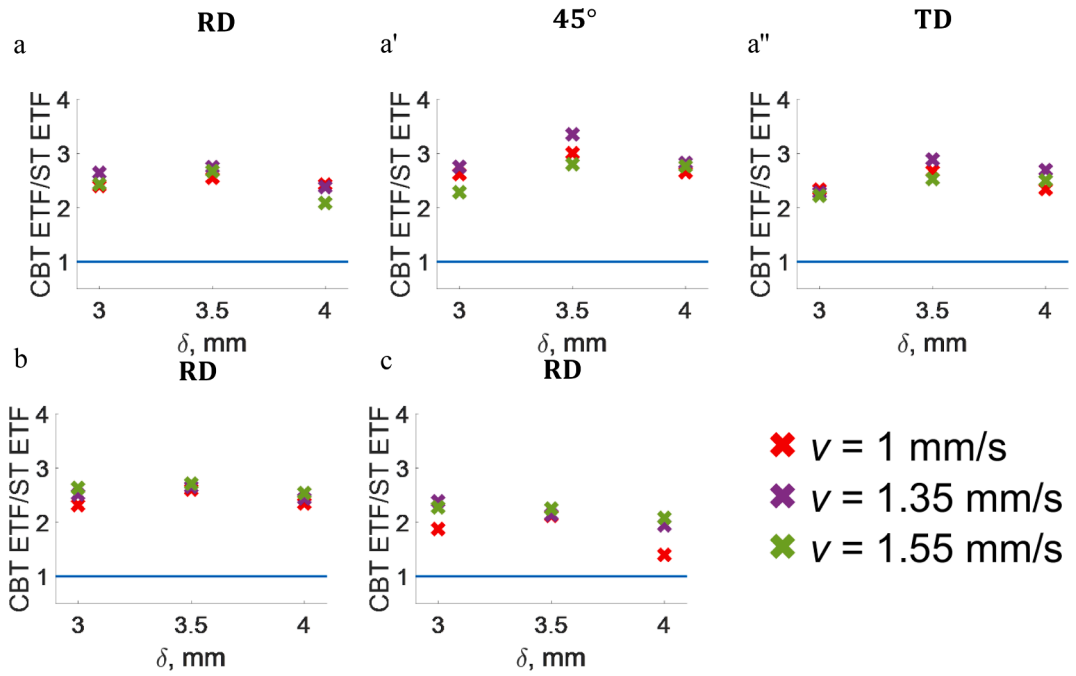

Fig. 8. Improvements in ETF by CBT of cp-Ti (grade 4): 1 mm thickness sheets along (a) RD, (a') TD, and (a'') 45°, (b) 1.3 mm thickness sheets in RD, and (c) 2 mm thickness sheets in RD. The data is normalized by ETF in ST, which is conservatively selected from multiple curves measured per direction.

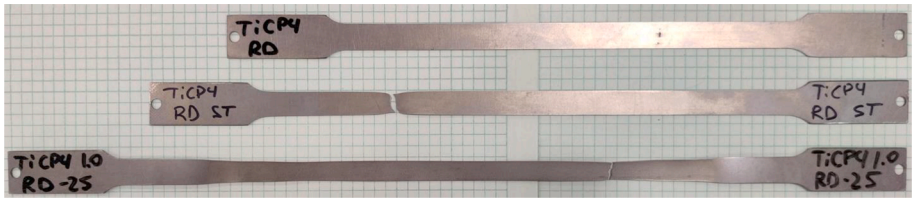

Fig. 9. A photograph showing an undeformed specimen (top), a fractured specimens in ST along RD under 0.001/s strain rate (middle), and a fractured specimens in CBT along RD under a pull speed of 1.35 mm/s and bending depth of 3.5 (bottom) at room temperature.

sheets, in addition to specimens like strips studied here. Details were presented in (Barrett et al., 2021). In summary, the apparatus consists of a moving carriage holding a specimen, a pair of grips, a pair of load cells (one at each grip) and a hydraulic actuator, a stationary roller assembly located on the bed, the bed holding a servomotor and a ball screw connected to the carriage to move it, and the software / hardware for data-collection. The hydraulic actuator is rated for 310 kN with a stroke of 305 mm. The capacity of donut-style load-cells is 22.24 kN. A program in LabVIEW controls and collects the axial loads from the load cells, crosshead displacement, and velocity of the carriage. The carriage reciprocated with a fixed 66 mm/s velocity, while the applied crosshead velocity is also constant but can take different magnitude per test. The carriage gets a signal from a limit switch to reverse after movement to the end of the stroke in each direction. A CBT cycle is defined as the rollers traversing the gauge length from one side to the other (one pass) and back from the other side to the original side (another pass). Clearly, the region of the sheet specimen close to the grips undergoes one bend/unbend per pass (1×), while the central region undergoes three bends/unbends (3×).

In a typical test, a constant crosshead pulling velocity is applied at one end of a test specimen, while the other end of the specimen is fixed. The resulting axial tensile force due to pulling ensures necessary wrapping of the sheet specimen around the rollers for the plastic flow taking place underneath or above the rollers. Axial motion of the rollers from one side of the specimen gauge section to the other imparts continuous bending/unbending of the test specimen simultaneously pulled in tension. The motion of the rollers provides incremental deformation region-by-region of the sheet specimen. This moving region experiences a combination of plastic bending and tension, while the rest of the sheet is in tension only elastically. The plastic deformation zone is solely underneath the rollers. The division of the specimen gauge length into the moving plastically deforming regions at the rollers from the rest of the specimen under elastic tension enables uniform elongation of the sheet to very large plastic strains, much larger than those possible in ST before necking. Therefore, ductility is depleted throughout the specimen gauge length under CBT circumventing necking at a single region followed by fracture intrinsic to ST. Concomitantly, the hardening is also relatively uniform in CBT throughout the sheet gauge length until small localization and fracture, as opposed to occurring locally in the neck after exhausting the uniform elongation under ST. Essentially, the specimen unloads with plenty of remaining ductility upon the necking event in ST. In contrast, the CBT test/process exploits nearly the entire ductility of the specimen. These general statements will be supported with photographs of tested specimens and more in depth descriptions later in the text. The parameters of the CBT process are bending depth and crosshead velocity. Sheet thickness can also vary. It should be appreciated that the stress/strain state caused by bending along with the stress/strain state caused by tension under CBT induces a combined tension/compression stress/strain profile that is non-symmetric. Moreover, the neutral axis moves towards the surface of the sheet up and down cyclically with cyclic bending.

The digital image correlation (DIC) was used to capture a full-field

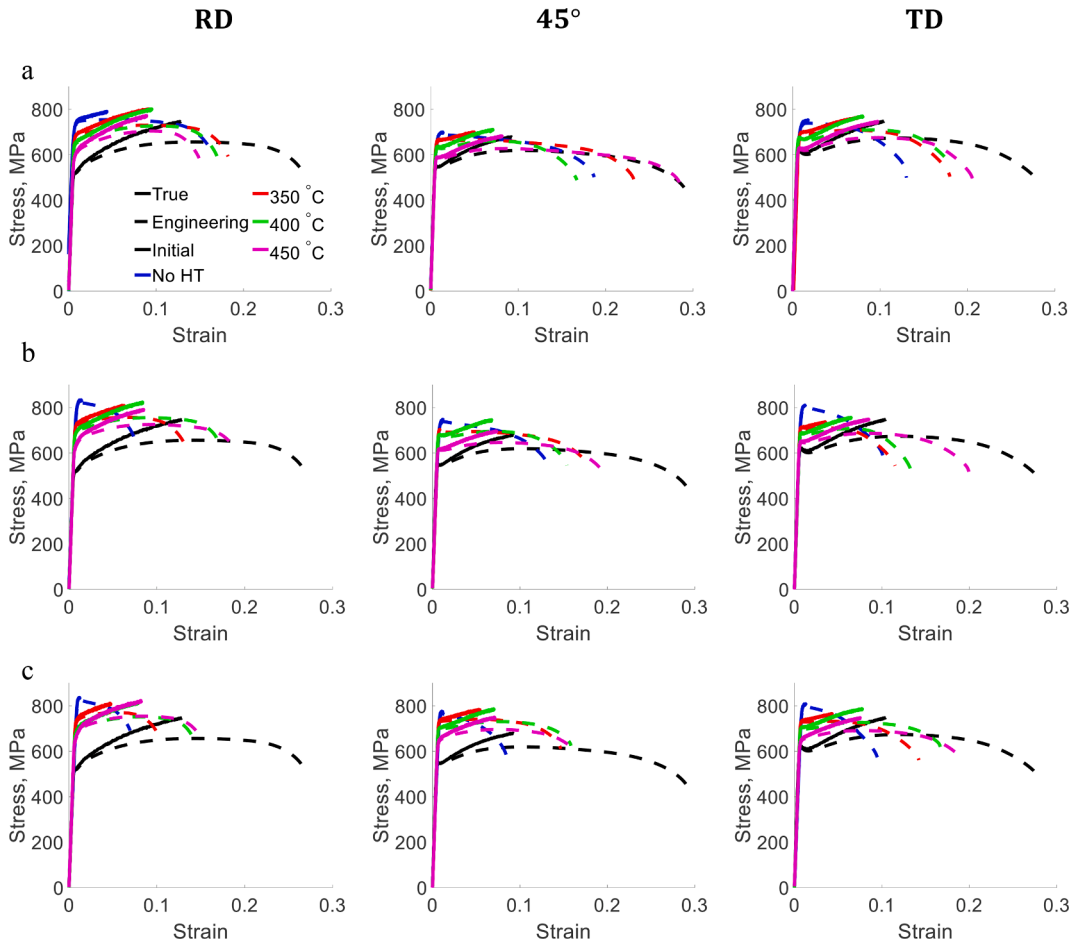

Fig. 10. Measured flow stress curves after testing sub-size specimens under 0.001/ strain rate at room temperature from 1 mm cp-Ti sheets treated by CBT only (at a pull speed of 1.35 mm/s and bending depth of 3.5) and treated by CBT using the same parameters + annealing for 1 h at the temperatures indicated in the legend: (a) CBT processing interrupted after 2 CBT cycles before cutting the sub-size specimens, (b) CBT processing interrupted after 6 CBT cycles before cutting the sub-size specimens, and (c) CBT processing interrupted after 10 CBT cycles before cutting the sub-size specimens. The plots include relevant measured curves of as-received (initial) cp-Ti (grade 4) material for reference.

two-dimensional axial strain profile of the specimen's top surface or the ND surface during one test for comparison with simulations to facilitate better understanding of the mechanics of the process. A speckle pattern was applied to an area of interest. A Rust-Oleum® high heat spray paint was used to create a speckle pattern, along with Krylon® matte finish spray coating to protect the surface from damage due to friction. A 16-megapixel camera with f/1.7 aperture was used to capture high contrast 4 K resolution at 60 fps video with the specimen surface illuminated by a secondary LED light. The camera had an auto-focus capability, which was utilized for the initial setup of the experiment. However, it was disabled during the experimental procedure. The camera was carefully positioned above the specimen and roller assembly at a fixed height, such that its optical axis was perpendicular to the middle of area of interest, enabling high-quality imaging. The camera's focus was between the specimen's gauge section and the grip attached to a hydraulic cylinder. The video was converted to an image sequence. The spatial resolution of the analyzed images in this study was 0.0391 mm/pix. One image was used as a reference for the initial spackle pattern, while the stretched images were used to obtain strain fields during the process and in particular after 2, 6, and 10 CBT cycles. The entire gauge section was not captured due to the roller's interference. The images were processed using VIC-2D DIC software of Correlated Solutions®. The software relied on the subset-based method since capable of tracking subsets in situations of large deformations and complex movements. An image was divided into small subsets and then each subset was compared to its counterpart in the reference image to determine its displacement. Normalized squared differences criterion for pixel matching along with subset size of 77 and step size of 5 parameters were chosen while running the software.

2.3. Annealing

A set of samples treated by CBT to given large strain levels underwent annealed to restore some of their ductility for trading off strength versus ductility. The annealing was performed using a Carbolite Gero GPCMA/37 furnace. Chamber of the furnace was preheated to a selected temperature prior putting specimens inside the furnace. K-type thermocouple was used to measure the temperature inside the chamber. The specimens were air-cooled to room temperature after one hour of HT. The purpose of annealing was to recover microstructure of the specimens and not to fully recrystallize them. 100 °C, 200 °C, 300 °C, 400 °C, 500 °C, and 600 °C temperatures were explored for partial annealing and then 350 °C, 400 °C, and 450 °C are selected for establishing tradeoffs in strength versus ductility for cp-Ti. Specimens were always held for one hour inside the furnace at all temperatures.

2.4. Characterization by EBSD and NeD

EBSD of cp-Ti was performed on a Pegasus system (Hikari High-Speed Camera and Octane Plus SDD detector) attached to a Tescan Lyra (Ga) scanning electron microscope (SEM). A detailed description of the electropolishing procedure for sample preparation for EBSD is given

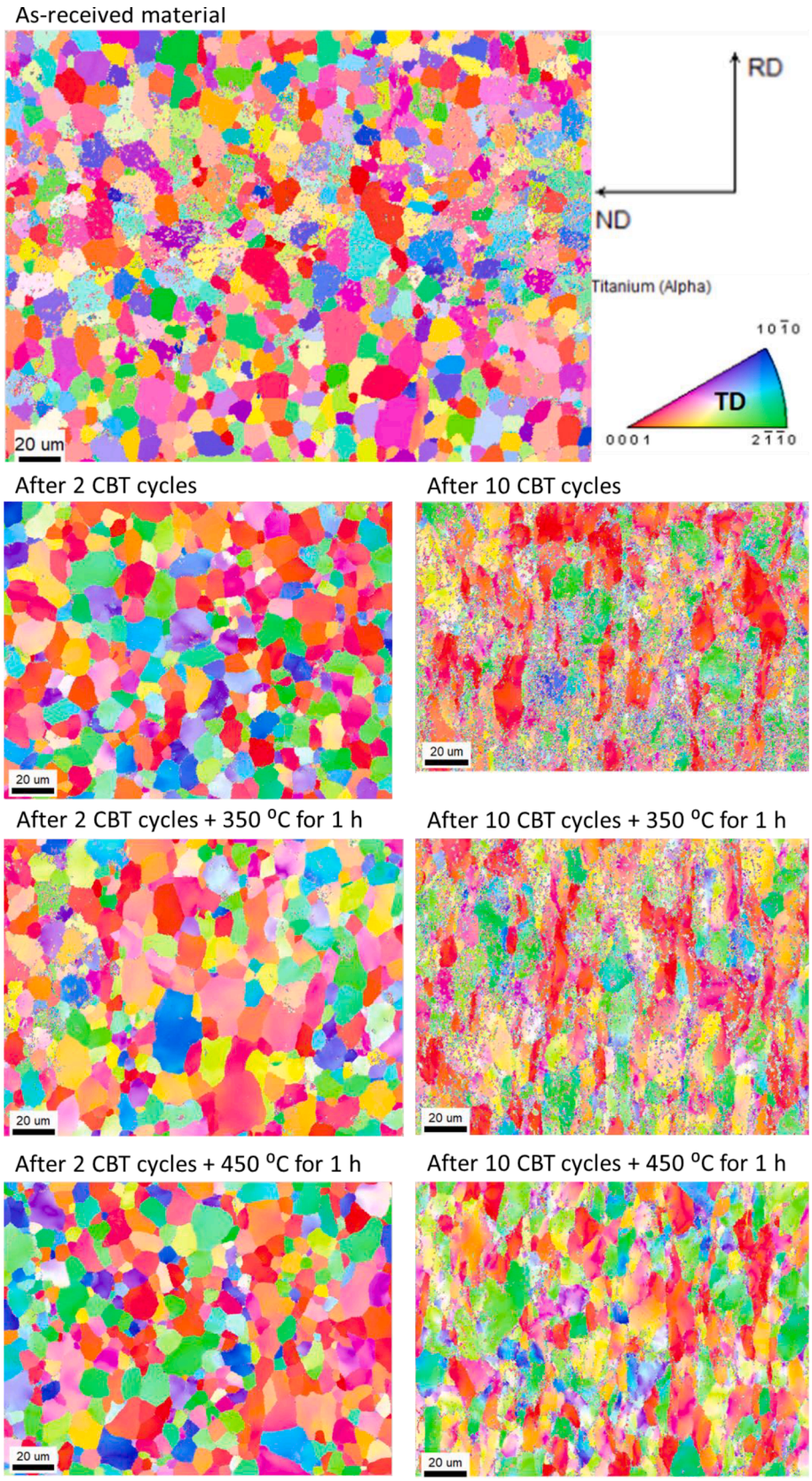

Fig. 11. IPF maps showing the evolution of grain structure during CBT along RD (at a pull speed of 1.35 mm/s and bending depth of 3.5) and annealing. The colors in the IPF triangle represent the orientation of the TD sheet axis relative to the frame of individual grains per map.

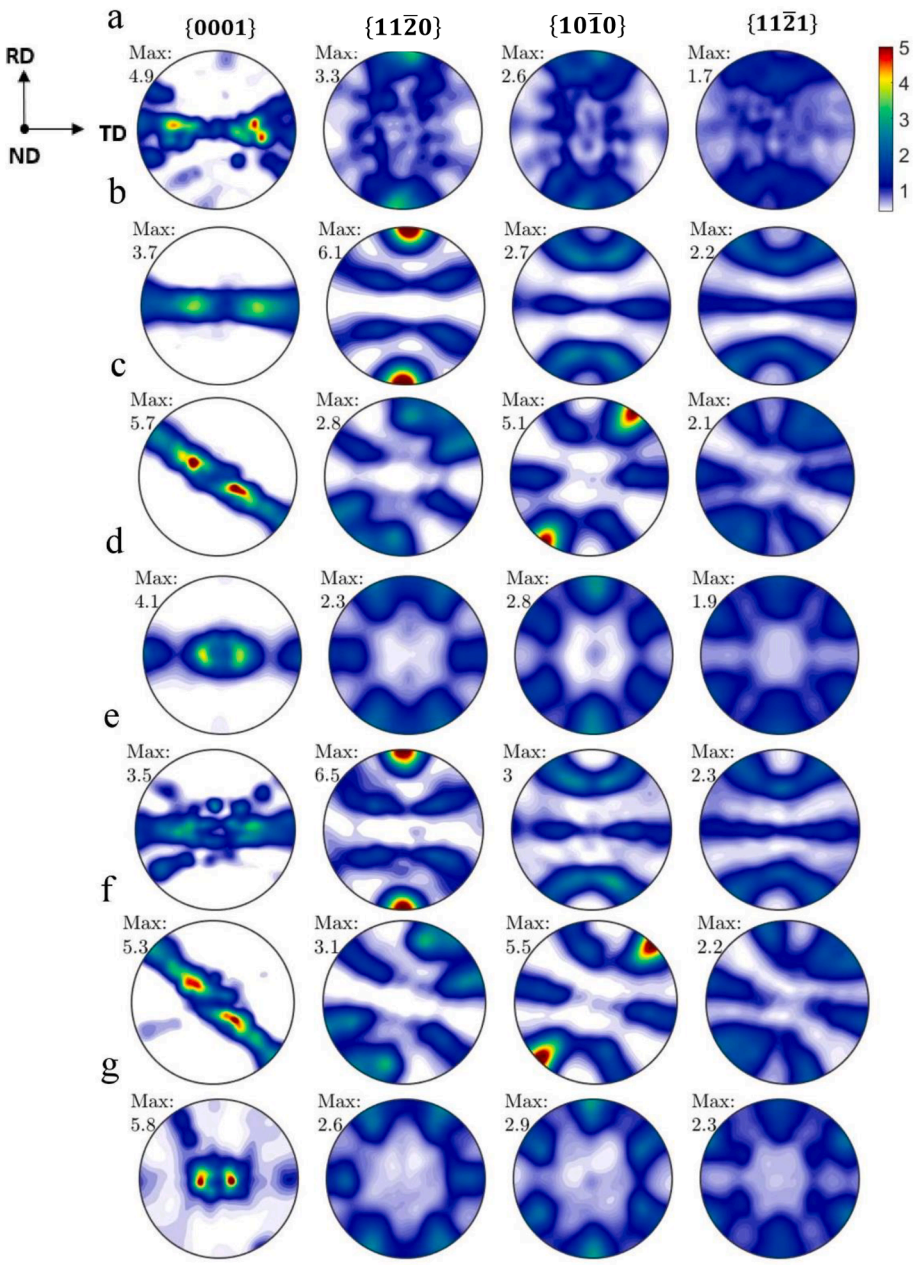

Fig. 12. Stereographic poles measured using NeD showing texture evolution in 1 mm thickness sheets of cp-Ti (grade 4): (a) initial texture, (b) ST to fracture along RD, (c) ST to fracture along 45°, (d) ST to fracture along TD, (e) 10 cycles CBT along RD, (f) 10 cycles CBT along 45°, and (g) 10 cycles CBT along TD. The CBT processing was performed under 3.5 mm bend depth and 1.35 mm/s crosshead velocity.

in (Ferreri et al., 2020; Knezevic et al., 2021; Riyad et al., 2021; Riyad et al., 2023).

Bulk texture measurements using NeD were performed in Los Alamos National Laboratory at their High Pressure Preferred Orientation beamline (Wenk et al., 2003). The count times were equivalent to around 30 min at a proton current of 100 micro-A. Inverse pole figures (IPF) were measured in 135 sample directions covering enough to fit an orientation distribution function (ODF) per specimen using the Rietveld refinement of the 135 patterns (Wenk et al., 2010). Rietveld refined orientation distribution functions was used to obtain corresponding pole figures per sample. The ODF analyses of the data were performed using MAUD (Wenk et al., 2010) with 7.5° resolution. Plotting of the poles was done in MTEX (Bachmann et al., 2010).

2.5. CBT simulation setup

The FE model created in Abaqus to simulate a CBT test is shown in Fig. 3. The model is for one half of the specimen because of the longitudinal symmetry of the specimen as well as because of rolling orthotropic texture symmetry of the sheet (Bhattacharyya et al., 2015; Knezevic and Kalidindi, 2007; Knezevic et al., 2008; Nasiri-Abarbekoh et al., 2012; Zecevic et al., 2016a), which will be shown later. Details pertaining to the mesh are provided in the figure caption. A mesh sensitivity study was performed to establish the mesh. The rollers are modeled as analytical rigid surfaces. The left end of the specimen is clamped, while the right end is pulled with a constant velocity as shown in the figure. The applied velocity is 1.35 mm/s, while the carriage velocity is 66 mm/s. To apply a bending depth, the top roller is lowered for 3.5 mm. The coefficient of friction for the hard contact between the

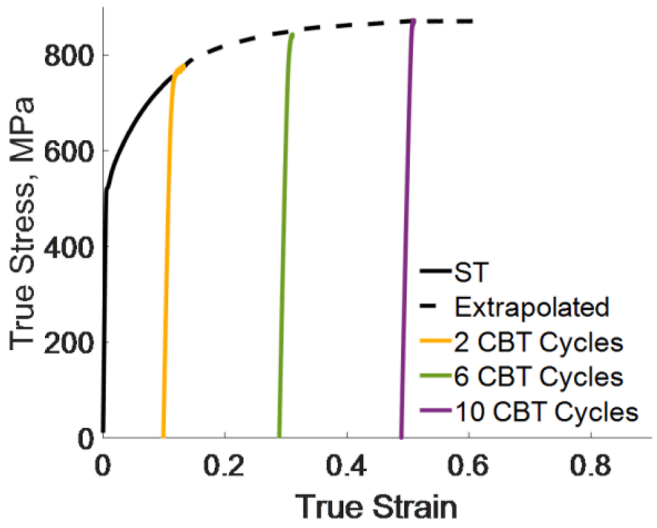

Fig. 13. Extrapolated flow curve for 1 mm thickness sheets of cp-Ti (grade 4) along RD based on shifting the flow curves from secondary ST tests for strain levels accumulated during CBT pre-straining to the given number of cycles.

Table 3
Accumulated strain during CBT pre-straining of 1 mm thickness sheets of cp-Ti (grade 4) along RD used to shift the flow curves from secondary ST.

# of cycles	$\mathcal{E}$	LE11	PEEQ
2	0.084	0.083	0.081
6	0.266	0.259	0.256
10	0.442	0.432	0.430

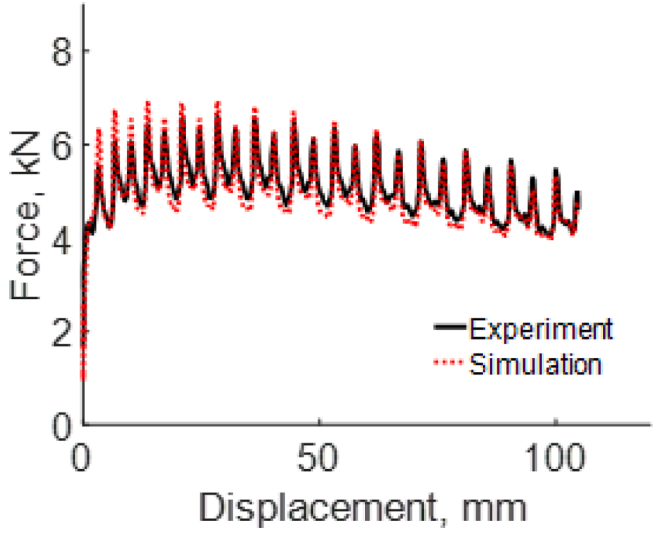

Fig. 14. Comparison of measured (black solid line) and simulated (red dotted line) force–displacement curves during CBT to fracture at 12.5 cycles under 3.5 mm bend depth and 1.35 mm/s pull speed of 1 mm thick cp-Ti (grade 4) sheets. (For interpretation of the references to color in this figure legend, the reader is referred to the web version of this article.)

rollers and the specimen is set to 0.1. Force to maintain the constant crosshead velocity and mechanical fields are predicted for comparison with corresponding experimental measurements to facilitate better understanding of the CBT mechanics. The von Mises yield criterion (i.e. the J_2 plasticity theory) is selected for the simulation.

3. Results

3.1. Experimental results

Fig. 4a shows measured true stress–strain curves for the as-received sheets of cp-Ti. The material shows some plastic anisotropy under tension with TD as the strongest direction. Interestingly, the TD direction shows upper and lower yield point, while the RD does not show it. The 45° direction shows similar behavior to TD but slightly softer. The uniform elongation of the material is slightly greater than 10% in every direction. The hardening is slightly more rapid along the softer RD than along the harder TD. Basic properties extracted from the curves are given in the appendix of the paper. The R-values for the as-received cp-Ti sheet of grade 4 in 0°, 45°, and 90° from RD were 1.26, 2.47, and 2.31. Fig. 4b shows the behavior of the material as a function of sheet thickness. The 2 mm sheets appear a bit stronger but show little less of uniform ductile than 1 mm and 1.3 mm sheets. The tests were repeated, and multiple curves per specimen category showed no visible differences. Fig. 5 shows the true stress–strain curves recorded during the strain rate jump tests. The SRS coefficients are given in Table 2. The material shows a moderate SRS along RD and slightly more along TD. Similar results were reported in prior literature (Lee et al., 2019). Given these results, the applied pull speed along with acceleration/deceleration at the beginning/end of passes can introduce some small effects on the recorded force–displacement data.

Fig. 6 shows representative load–displacement curves measured under CBT along RD for cp-Ti sheets. The curves in Fig. 6a are for four bending depths and those in Fig. 6b are for four crosshead velocities. The load–displacement curve recorded under ST is shown for reference in both plots. Evidently, the ETF is substantially enhanced using CBT over the ST. The extent of the enhancement varies with the selected set of process parameters. Moreover, the axial forces are lowered during CBT relative to that under ST. As more deformation is caused by bending than tension the tensile force decreases in magnitude. The greater the imposed banding depth causing the greater amount of bending, the lower the axial force. Similarly, the slower the pull speed the lower the axial force because of more bending. Therefore, the magnitude of force is driven by the tradeoff between the amount of tension versus the amount of bending involved in the plastic deformation. The characteristic periodic pattern of spikes and plateaus is evident from the CBT load–displacement curves, while the ST curve exhibits the typical decreasing work hardening. The peaks during CBT arise when the rollers are decelerating/accelerating. Stopping of the rollers means no bending deformation but pure ST conditions at the maximum of the peaks. Heights and periods of the spikes are in function of process parameters. Increase in the bending by the increase in the bending depth and the consequential increase in the bending strain/stress implies the lower required tensile strain/stress to deform the specimen and the higher amplitude of the peaks with nearly constant periods for a fixed pull speed. Increase in the pull speed implies that the sheet is pulled faster during CBT causing the peaks to be more spread i.e. the periods are broader and also the strain rate is higher. The more stretched peaks imply that the sheet is under reduced amount of bending because the bending deformation occurs only under/above the rollers. The bending conditions must not under-bent or over-bent the sheet to be optimal. The sheet is under greater tension if under-bent, which will likely reduce ETF. Bending stresses/strains are high if over-bent causing also lower ETF. Therefore, optima are sought.

Fig. 7 shows the load–displacement curves as a function of thickness for a consistent set of process parameters. Evidently, the 1 mm sheet of cp-Ti can be stretched more under CBT than the thicker sheets. The thickest sheet of 2 mm fails first under the given process parameters. As explained above, the combination of bending and pure tensile stresses under CBT induces a non-symmetric stress / strain profile with the neutral axis cyclically shifting towards the sheet surfaces touching the roller over which the sheet is passing. The location of neutral axis

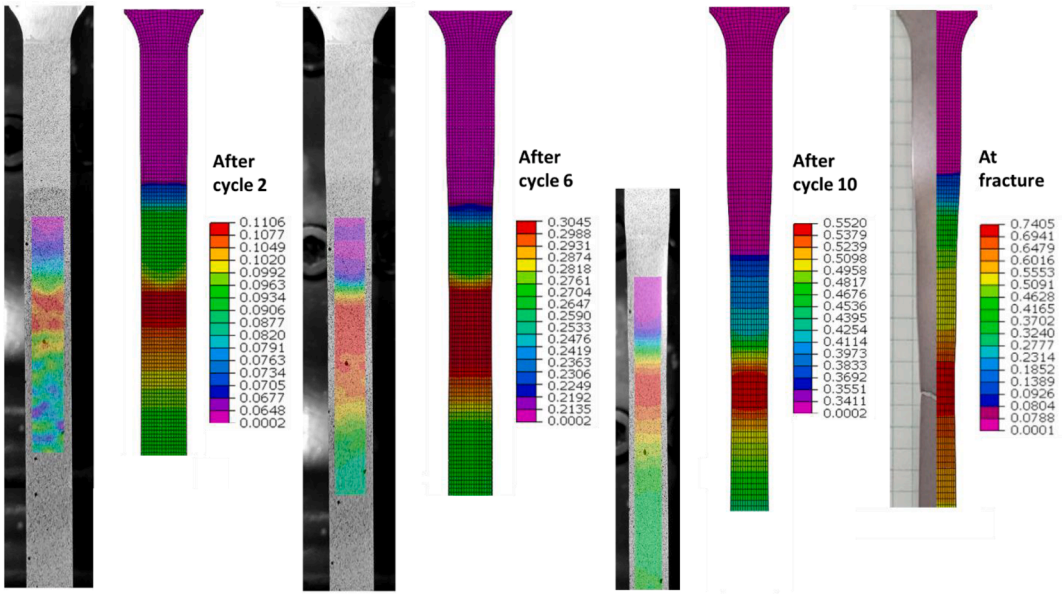

Fig. 15. Comparison of measured strain fields by DIC (e_{yy} - Hencky) and predicted strain fields by the simulation in Abaqus (LE11) after a given number of CBT cycles to fracture (12.5 cycles) of cp-Ti (grade 4) 1 mm thickness sheets. The CBT process parameters were 3.5 mm bend depth and 1.35 mm/s pull speed. The same legend applies for both experimental measurements and simulations at a given number of CBT cycles.

Fig. 16. Experimentally deformed specimen in CBT to fracture from Fig. 9 in comparison to the corresponding specimen from the FE simulation showing the axial strain contours from Fig. 15. The color intensity legend is the same as in Fig. 15 at fracture.

depends on the sheet thickness. The more it is inside the sheet the better conditions for achieving the greater ETF. The addition of the bending tension to the pure tension produces the greatest stress i.e. the plastic flow stress of the material on the outward edge of the sheet on the opposite side of the touching roller. The thicker the sheet the easier to reach the flow stress at the outward edge. The side of the sheet touching the roller is in compression. The aspect is also enhanced with the sheet thickness. This compressive portion of the axial stress profile is a stabilization facilitated by CBT, which will be discussed later. The achieved ETF varies with sheer thickness compromising the maximum axial stress and the stabilization. The sheet during CBT undergoes thinning. The extent of specimen thinning can go to the point of the neutral axis (i.e. the offset from the specimen middle owing to the combined bending and tension) leaving the interior of the specimen. If this takes place, the entire specimen is in tension. Under such condition the specimen would behave similar to a tension test so that the remaining hardening / ductility quickly gets exhausted, and the specimen fails. The behavior of the neutral axis can also be influence by the presence of any Bauschinger effect (BE) in the tested material under CBT (Bauschinger, 1886; Revil-Baudard et al., 2021).

Fig. 8 presents the results of a comprehensive parametric study into ETF in function of bending depth and pull speed. An additional plot containing more data is presented in the appendix of the paper. Based on the figure provided in the appendix, three pull speeds and three bend depts are selected in the search of the most optimal parameters shown in Fig. 8. The pull speed of 1.35 mm/s and the bending depth of 3.5 mm are nearly the most optimal parameters based on the discrete data shown in Fig. 8 for achieving the greatest ETF of cp-Ti along every direction for 1 mm and 1.3 mm sheets. Due to greater bending for the thicker 2 mm sheet given the same parameters as for the thinner sheets, the results show that optimal bending depth for 2 mm sheets is slightly below and closer to 3 mm. The figure also shows that thicker sheets may benefit a bit from slightly increasing the speed to 1.55 mm/s. Nevertheless, most of the data in Fig. 8 can be regarded as acceptable ranges of parameters for achieving enhanced ETF.

Fig. 9 shows photographs of a specimen failed in ST in comparison with a specimen failed in CBT under a given set of process parameters. An undeformed specimen (top) is also shown as a reference to appreciate the ETF in ST versus CBT. Evidently, the outcome of CBT on ETF is considerable. Necking is evident after inspecting cp-Ti specimens tested to fracture in ST, as shown in the figure for one of them. Remaining ductility surrounding and away from the necking region can be exploited by CBT, as this work is showing. The available deformation in the sheet to deplete after exhausting the uniform elongation is more for materials exhibiting more necking. CBT minimizes the localization of plastic deformation and the appearance of necking. Essentially, the CBT deformation inhibits the appearance of necking because ductility is depleted as uniformly as possible along the specimen. Hence the plastic deformation proceeds to large plastic strains, while depleting the ductility uniformly along the specimen. Ultimately, the allowable deformation of the material under CBT is achieved, at which point the plasticity quickly localizes and the material breaks. Specimens in CBT fail with minimal necking.

Fig. 10 shows measured true stress–strain and engineering stress–-strain curves based on testing the sub-size specimens of sheets processed using CBT to a certain uniform strain as a consequence of the given number of CBT cycles. The processing by CBT was under 1.35 mm/s crosshead velocity and 3.5 bending depth. As evident from the engineering curves, the tested materials interestingly exhibit prolonged falling portion of the curves beyond ultimate tensile strength (UTS). The

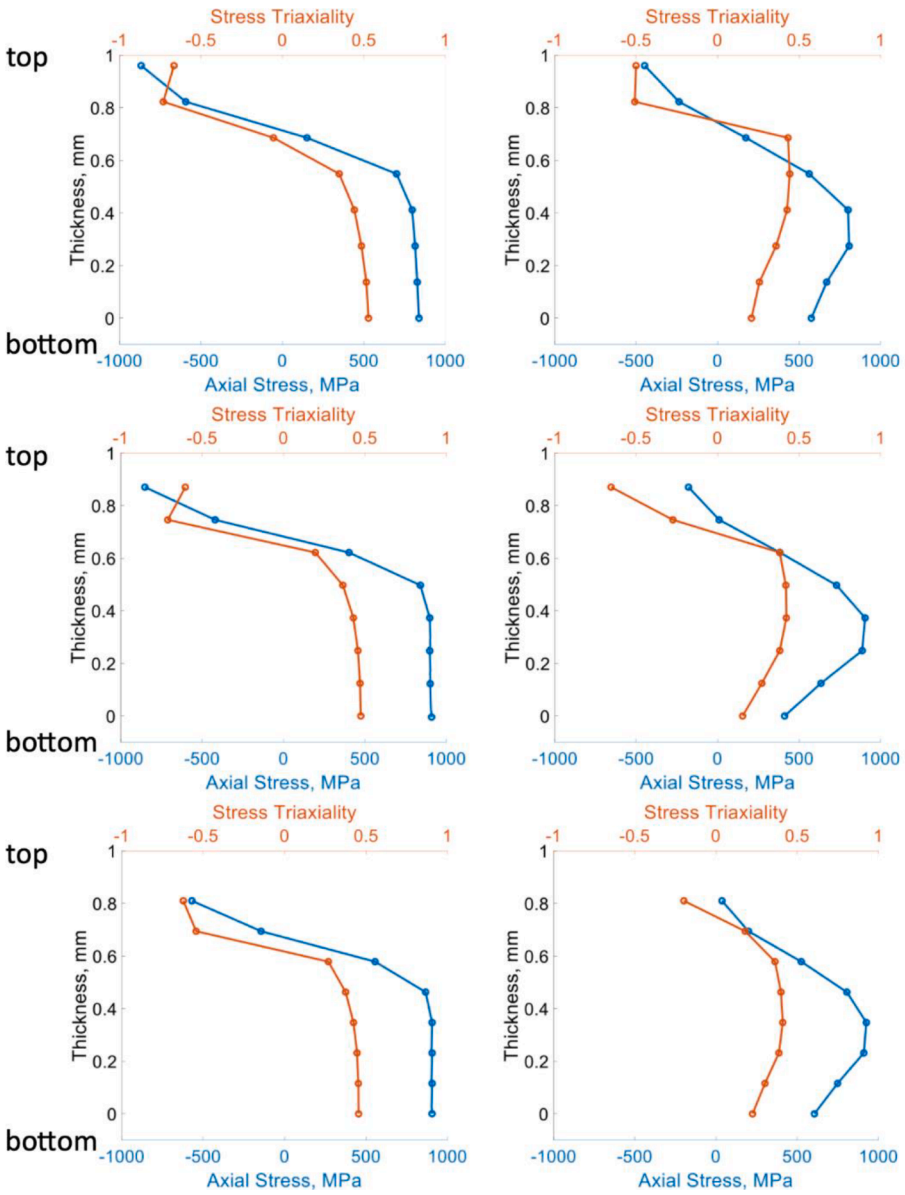

Fig. 17. Axial stress and triaxiality profiles developed through-thickness in 1 mm thick sheets of cp-Ti (grade 4) with CBT cycles (2 top, 6 middle, and 10 bottom two sub-images) at 3.5 mm bend depth and 1.35 mm/s pull speed underneath the top roller (left) and in the gauge section of the specimen away from the rollers (right).

sub-size specimens were consistently cutout from the 3× region of the CBT specimens. The purpose of these tests was to evaluate increases in strength and the extent of residual ductility in the material per test direction upon the CBT processing. To appreciate the increases in strength and reductions in ductility, the curves for the as-received (initial) cp-Ti are shown per test direction. The results reveal that the strength of the material can substantially increase over the as received material by processing it with CBT at the expanse of residual ductility. Strength of the material was found to increase by a factor of 1.3 along the sheet strongest direction, while by a factor of 1.6 along the sheet softest direction with 10 CBT cycles reducing the anisotropy. Given the uniform elongation facilitated by CBT to very large strains, tradeoffs in strength and ductility of the material were examined next by subjecting a set of sheet specimens processed to 2, 6, and 10 CBT cycles under the optimized parameters to annealing. The load–displacement for these pre-strains going far beyond those achievable in ST are provided in the appendix. Sets of CBT specimens were annealed at 350 ºC, 400 ºC, and 450 ºC for recovery and then sub-size specimens were made of the annealed materials for testing. The figure shows interesting tradeoffs. Importantly, the ductility of ∼ 5% could be restored by annealing the material at 350 ºC for one hour, while preserving high strength and isotropy. The quantitative data of mechanical properties are extracted from the curves and provided in the appendix.

Grain structures of cp-Ti beginning from the initial to deformed under CBT along RD and TD to 2 and 10 CBT cycles were characterized using EBSD. Fig. 11 shows the IPF maps in the RD-ND plane for the deformed material in RD, while the appendix presents the maps of the material deformed in TD. No cleaning was applied to the maps presented in this paper. The red color in the maps in Fig. 11 indicates that the TD sample axis is nearly perpendicular to basal planes for a large fraction of grains i.e. the crystal **c**-axes of these grains is closely aligned with the TD axis of the sample. The fraction of prismatic planes perpendicular to TD is increasing with strain during CBT cycles. Grains elongate morphologically with plastic strain along the pull direction imparted by CBT and develop orientation spreads as a consequence of crystallographic slip with very little deformation twinning present in the deformed structures. The figure also shows the evolution of grain structure during annealing. The orientation spreads reduce with annealing due to

Table A1
Young's modulus (E, GPa), yield strength (YS, MPa), ultimate-tensile strength (UTS, MPa), uniform strain, and strain at fracture estimated from the flow curves in Fig. 10.

Name	Direction	E, GPa	YS, MPa (0.2% offset)	UTS, MPa	Eng. Strain at UTS	Eng. Strain at Fracture
As Received	RD	108	507	657	0.1395	0.267
After 2 CBT cycles	RD	114	722	755	0.0427	0.1653
After 2 CBT cycles + HT (350 °C)	RD	113	678	731	0.0865	0.1832
After 2 CBT cycles + HT (400 °C)	RD	119	645	728	0.1007	0.1705
After 2 CBT cycles + HT (450 °C)	RD	113	591	704	0.0945	0.1502
After 6 CBT cycles	RD	107	785	822	0.0120	0.1066
After 6 CBT cycles + HT (350 °C)	RD	109	720	758	0.0666	0.1345
After 6 CBT cycles + HT (400 °C)	RD	113	683	750	0.0816	0.1691
After 6 CBT cycles + HT (450 °C)	RD	109	626	725	0.0930	0.1856
After 10 CBT cycles	RD	101	803	812	0.0100	0.0705
After 10 CBT cycles + HT (350 °C)	RD	104	731	771	0.0497	0.1029
After 10 CBT cycles + HT (400 °C)	RD	110	681	756	0.0785	0.1538
After 10 CBT cycles + HT (450 °C)	RD	108	659	755	0.0801	0.1506
As Received	45°	118	544	619	0.0995	0.2928
After 2 CBT cycles	45°	118	658	689	0.0108	0.1882
After 2 CBT cycles + HT (350 °C)	45°	119	656	667	0.0555	0.2340
After 2 CBT cycles + HT (400 °C)	45°	116	627	661	0.0731	0.1682
After 2 CBT cycles + HT (450 °C)	45°	113	584	627	0.0777	0.2854
After 6 CBT cycles	45°	108	720	738	0.0111	0.1350
After 6 CBT cycles + HT (350 °C)	45°	104	690	698	0.0124	0.1767
After 6 CBT cycles + HT (400 °C)	45°	107	671	695	0.0681	0.1548
After 6 CBT cycles + HT (450 °C)	45°	108	612	646	0.0747	0.1991
After 10 CBT cycles	45°	109	746	758	0.0102	0.0856
After 10 CBT cycles + HT (350 °C)	45°	110	730	741	0.0439	0.1479
After 10 CBT cycles + HT (400 °C)	45°	109	696	730	0.0711	0.1598
After 10 CBT cycles + HT (450 °C)	45°	111	645	696	0.0722	0.1636
As Received	TD	118	601	675	0.1208	0.2789
After 2 CBT cycles	TD	114	686	739	0.0182	0.1314
After 2 CBT cycles + HT (350 °C)	TD	117	664	709	0.0667	0.1811
After 2 CBT cycles + HT (400 °C)	TD	119	659	708	0.0887	0.1788
After 2 CBT cycles + HT (450 °C)	TD	117	619	676	0.0954	0.2069
After 6 CBT cycles	TD	118	780	800	0.0107	0.1021
After 6 CBT cycles + HT (350 °C)	TD	111	706	710	0.0629	0.1531
After 6 CBT cycles + HT (400 °C)	TD	114	680	703	0.0682	0.1338
After 6 CBT cycles + HT (450 °C)	TD	116	645	687	0.0868	0.2007
After 10 CBT cycles	TD	108	792	800	0.0115	0.0958
After 10 CBT cycles + HT (350 °C)	TD	109	727	732	0.0410	0.1434
After 10 CBT cycles + HT (400 °C)	TD	108	698	728	0.0752	0.1686
After 10 CBT cycles + HT (450 °C)	TD	109	645	691	0.0761	0.1905

recovery processes. While the quality of the IPF maps shows the extent of recovery indirectly, the appendix provides the corresponding kernel average misorientation (KAM) maps to better depict the extent of recovery. Essentially, the sheets after 1 h at either 350 °C or 400 °C or 450 °C have similar grain structure like the sheets after the CBT processing only. Therefore, merely different extent of recovery occurred in the samples with more at the higher temperature and with no evidence of partial recrystallization.

Pole figures in Fig. 12 show the texture evolution during ST and CBT

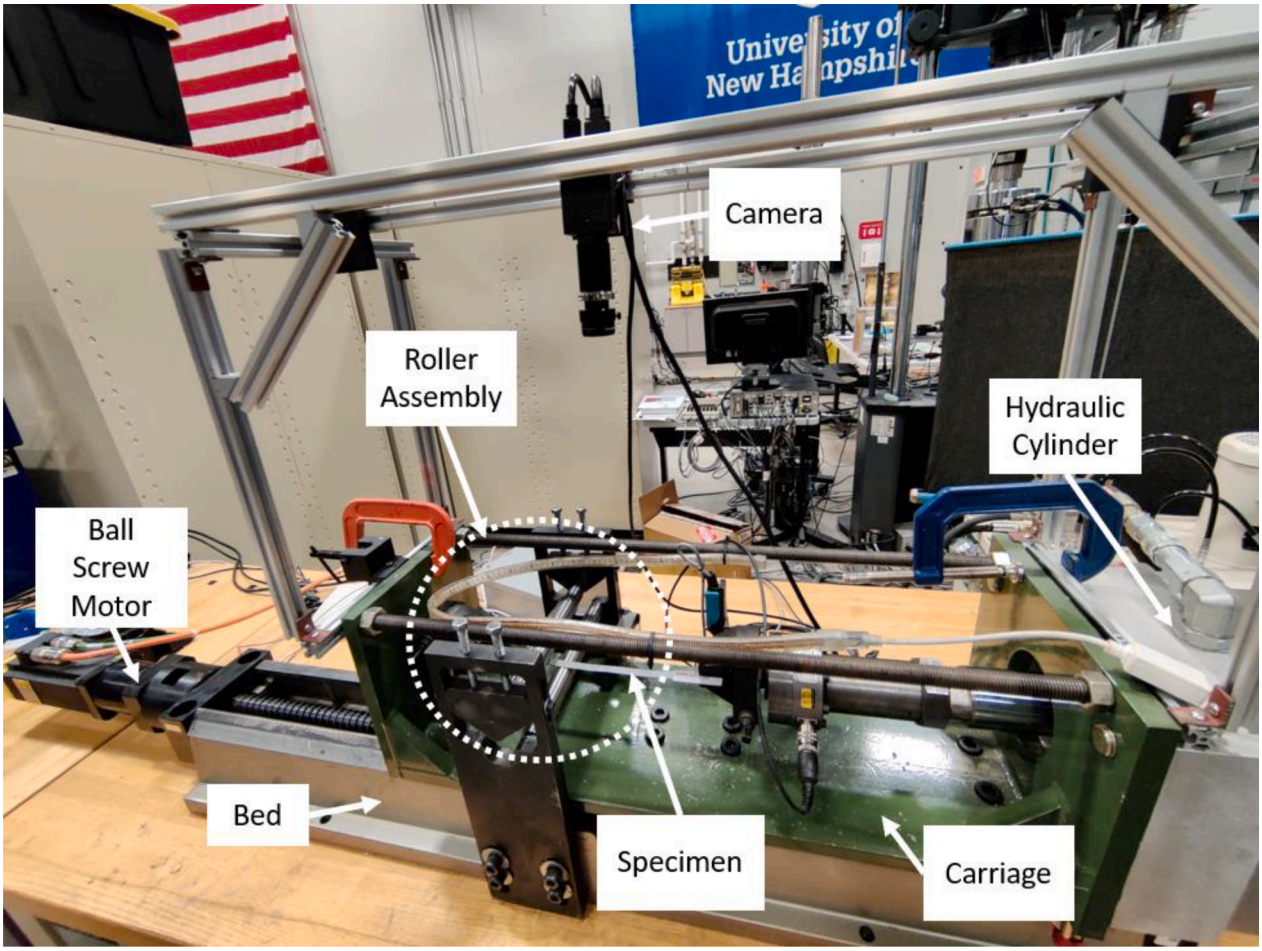

Fig. A1. A photograph of the CBT tester. The main components are identified in the photograph.

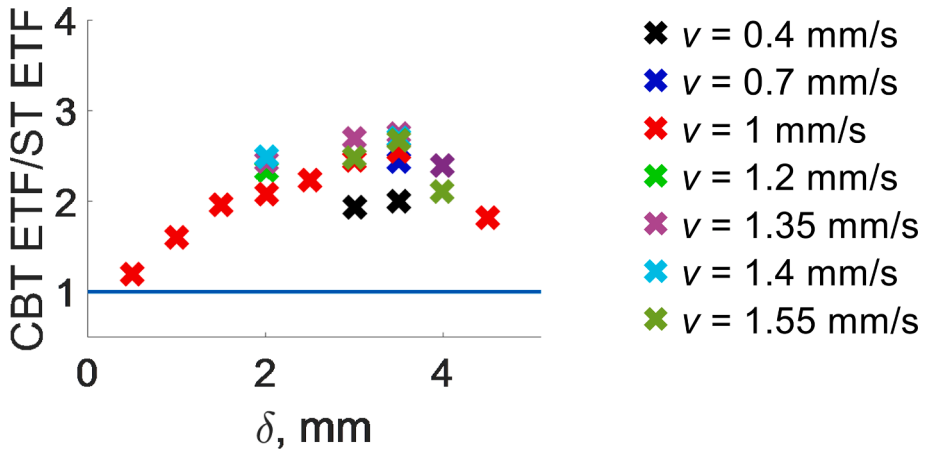

Fig. A2. More data points added to Fig. 8a.

from the initial texture in the as-received sheet. The initial texture is a moderately strong basal texture tilted in the TD, as reported in prior literature (Luan et al., 2018; Wang et al., 2018). Texture evolution in CBT is like the texture evolution in ST signifying similar stress/strain state in the sheets in CBT and ST. However, the intensities are higher in CBT because of higher strain levels attained in CBT than in ST. Besides the formation of the pronounced prismatic pole along RD axis no substantial texture change from the initial texture occurs in tension along RD. Realignment of the basal intensities at 45° along with the formation of the prismatic pole with the pull direction is noticeable under tension in 45° between RD and TD. Some texture evolution also occurs in tension along TD, where the spread of basal poles reduces and distinct peaks form approximately 15° from the ND. Some realignment of intensities in the prismatic and pyramidal poles under tension in the TD is also noticeable. The texture evolution in cp-Ti under ST and CBT are gradual implying the slip dominated deformation. Prismatic slip primarily and basal slip secondary are expected to dominate the deformation, which is common for Ti (Knezevic et al., 2013; Knezevic et al., 2010; Knezevic

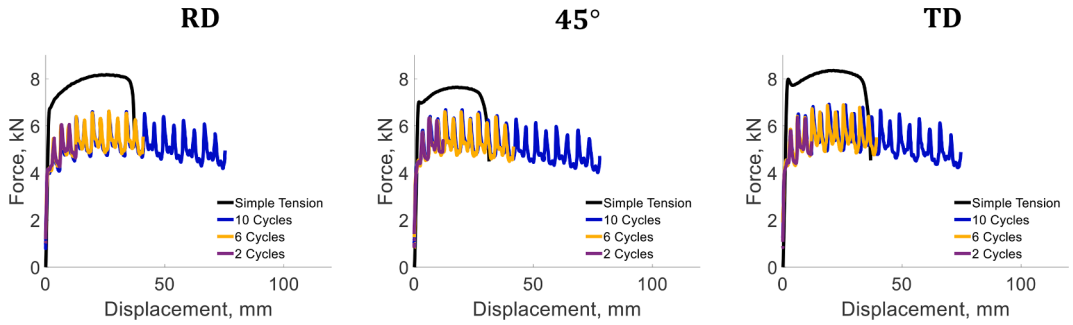

Fig. A3. Measured force–displacement curves during pre-straining of the specimens to 2, 6, and 10 CBT cycles under 3.5 mm bend depth and 1.35 mm/s pull speed. Measured force–displacement curves in ST are shown for reference.

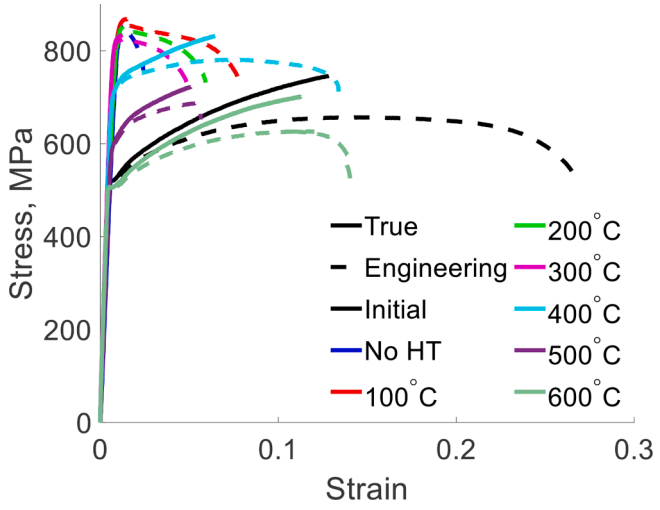

Fig. A4. Measured flow stress curves after testing sub-size specimens under 0.001/ strain rate at room temperature from 1 mm cp-Ti sheets treated by CBT to 10 cycles at a pull speed of 1.35 mm/s and bending depth of 3.5 and then annealed for 1 h at the temperatures indicated in the legend. These results are used to select HT temperatures for the results presented in Fig. 10.

et al., 2015; Wang et al., 2020; Wu et al., 2007). Since some fractions of grains are oriented in a way that their **c**-axes are compressed along with negligible fraction of tensile twinning, the compressive strain in the **c**-axes direction must be accommodated by some pyramidal slip. The improvements in strength stem from the buildup of dislocations due to cold work.

3.2. Simulation results

Although an FE simulation of the CBT process was numerically challenging given relatively complex kinematics and large plastic strains, the entire test to 12.5 CBT cycles was successfully simulated in Abaqus. The simulation was carried out using the plasticity theory of von Mises (Abaqus, 2017) (i.e. the J_2 plasticity) based on the true stress-true strain curve of cp-Ti along RD. While accurate modeling of multi-axial deformation of cp-Ti requires more advances yield criteria given that the material exhibits some anisotropy and tension–compression asymmetry (Baral et al., 2018; Hama et al., 2015), the present work assumed the von Mises yield criterion because only one direction of the sheet is tested under tension. Future works will attempt to develop a more accurately model for cp-Ti based on crystal plasticity theory (Zecevic and Knezevic, 2015; Zecevic and Knezevic, 2017; Zecevic et al., 2021; Zecevic et al., 2017b) for modeling of complex multi-axial deformation of the material. Fig. 13 shows the cp-Ti flow curve provided to Abaqus for the simulation of CBT. The curve was appropriately extrapolated based on the curves obtained from testing in ST of three pre-strained specimens to 2, 6, and 10 CBT cycles. The secondary curves were appropriately shifted for the accumulated axial strain during pre-straining. The extrapolation procedure was presented first in (Barrett and Knezevic, 2020). The accumulated strain for the shifts was estimated by establishing a gauge length, l, of the CBT specimen, which is the length that the carriage delineates, $l = \int v_r dt$ and the specimen elongation because of the crosshead motion for $dl \approx \Delta l = \int v_c dt$ The integrals were evaluated numerically using the experimentally measured profiles to obtain the strain increment per pass as $\Delta\varepsilon = \frac{\Delta l}{l} = \frac{\int v_c dt}{\int v_r dt}$ The total strain after a given number of CBT cycles is then a sum of the increments in strain per pass. The strain levels were also taken from the simulation. Table 3 compared the estimated strain levels for 2, 6, and 10 CBT cycles to shift the measured curves. Given that the axial strain component (LE11) and the equivalent plastic strain (PEEQ) i.e. the integral along the path are similar in magnitude additionally verifies the uniaxial strain/stress state in the sheet during CBT, which was also evident from similar texture evolution in ST and CBT. The delineated curve based on the secondary tests was used as a guess to predict the load–displacement curve and was regarded as good after successfully reproducing the load–displacement measured curve. Fig. 14 shows the comparison. Evidently, the model predicts the succession of spikes and plateaus inherent to the CBT load–displacement curve verifying the extrapolated stress–strain curve.

4. Discussion

This paper described results from a detailed investigation into the influence of CBT and annealing on improving ETF and optimizing strength and ductility of cp-Ti. The CBT process facilitated uniform deformation of cp-Ti to greater strain levels than achievable under ST owing to the incremental plastic deformation taking place underneath the rollers and stabilizing mechanical fields in the sheet. The work showed markedly positive influence of CBT on ETF and axial load levels, especially under the optimized bend depth and pull velocity. Under a normalized bend depth of 3.5 and a pull speed of 1.35 mm/s, the ETF of cp-Ti improved from 2.9× to 3.5× depending on the selected test direction. These improvements are better than those obtained for aluminum alloys (Zecevic et al., 2016c) and are similar to those obtained for dual-phase steels (Poulin et al., 2019; Poulin et al., 2020b). The hardening in ST of cp-Ti was evenly depleted until necking as in other materials. After the necking localization occurred, the neck commonly begun to accumulate any subsequent plastic strain beyond the uniform, while the rest of the specimen unloaded with a lot of remaining capacity to deform. CBT extended the uniform hardening to greater strain levels because CBT suppressed necking. In essence, the purpose of CBT process was to deform sheets of cp-Ti uniformly while exploiting ductility of the entire gauge section to much larger extents than possible in ST.

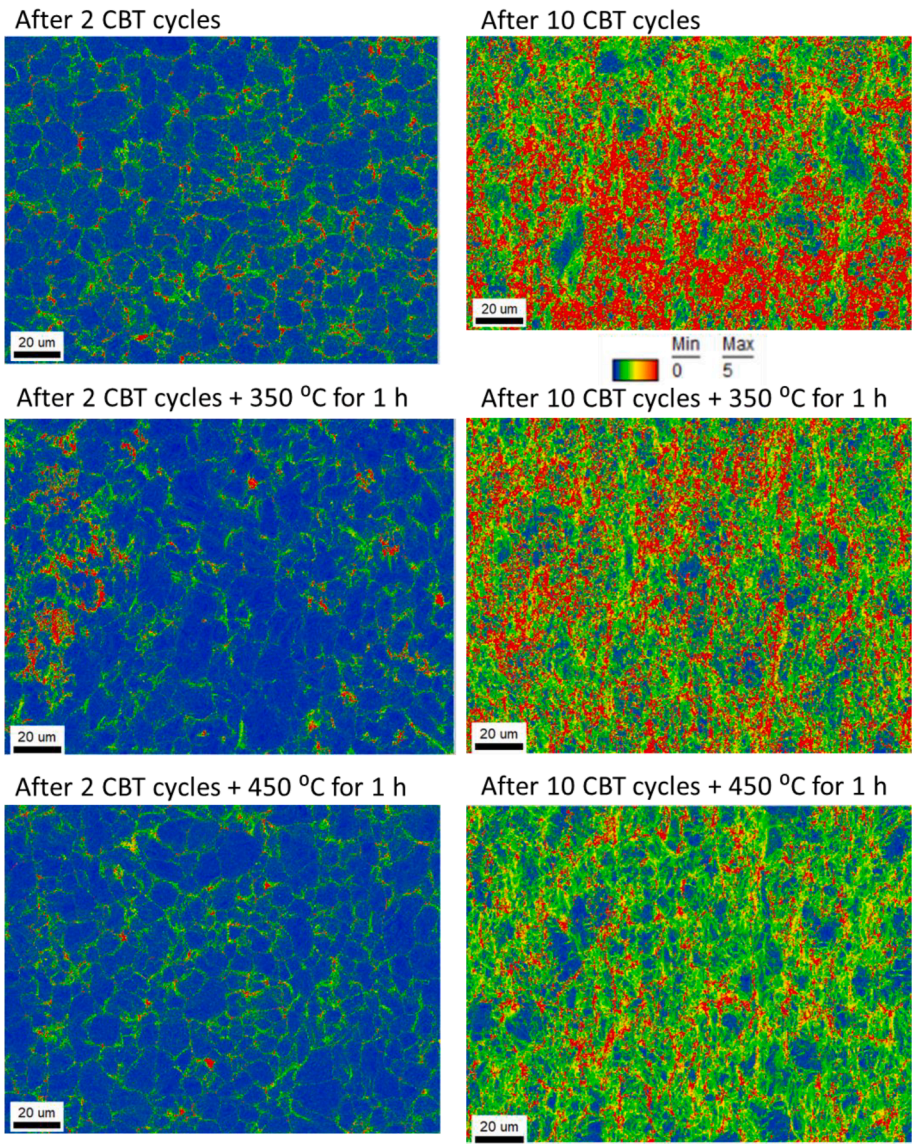

Fig. A5. KAM maps based on the maps from Fig. 11 showing the evolution of misorientation trends during CBT along RD and annealing.

Importantly, the remaining ductility in cp-Ti was substantial such that the improvements in ETF by CBT were also substantial.

The work showed not only that ETF of cp-Ti can be substantially improve by CBT but also that the strength and residual ductility can be treaded off by CBT and annealing. Strength of cp-Ti was found to increase by a factor of 1.3 along the sheet strongest direction, while by a factor of 1.6 along the sheet softest direction with 10 CBT cycles. Ductility of ~ 5% could be restored by annealing the material at 350 °C for one hour, while preserving nearly isotropic behavior. Interestingly, the material does not have the previous anisotropy after CBT given more rapid hardening along RD than TD and the underlying texture changes. The characterization of texture evolution for cp-Ti revealed expected texture evolution under tension with slightly higher intensities under CBT than ST. Given some changes in grain morphology and some grain refinement with minor activity of twinning in the structure after CBT, the strength increase was owing to the increase in density of dislocation. Appendix presents a set of KAM maps as indirect measures of dislocation density. The deformation under tension of cp-Ti was dominated by prismatic and basal slip systems, and some minor contribution of pyramidal slip (Savage et al., 2021b; Savage et al., 2021b; Zecevic et al., 2017a). Finally, the measured SRS for cp-Ti was consistent with the literature of Ti alloys (Lee et al., 2019).

The FE simulation of the CBT process performed to predict load–displacement and verify the extrapolated stress–strain curve of cp-Ti was used to determine the stress and strain fields developing during the process. The model successfully predicted the axial strain along the sheet and elucidated the location and onset of failure. Fig. 15 presents a comparison of measured axial strain fields by DIC and predicted axial strain fields during the CBT test to 12.5 cycles. More measured DIC images are provided in the appendix. The model captures the axial strain profile in the width direction. The specific profile is commonly observed and attributed to the edge effect. The strain/stress in the width direction is decreasing from the center of the strip to zero at the free edge. While the edge is free in the width direction, axial strain/stress exists across the entire width. Fig. 16 compares the experimentally deformed specimen from Fig. 9 and the simulated specimen from Fig. 15 at 12.5 cycles. The predicted localization region between 2× and 3× deformation regions is the location of fracture. The location of fracture is where the rollers stop and restore the most severe tensile deformation. As the rollers stop moving axially, the region of the specimen underneath the inner roller is submitted to the maximum tension corresponding to the peaks in load–displacement and an additional from the roller curvature. As the rollers start moving in the other direction, the process ceases. Nevertheless, the instant of rollers stopping is sufficient to induce some surplus

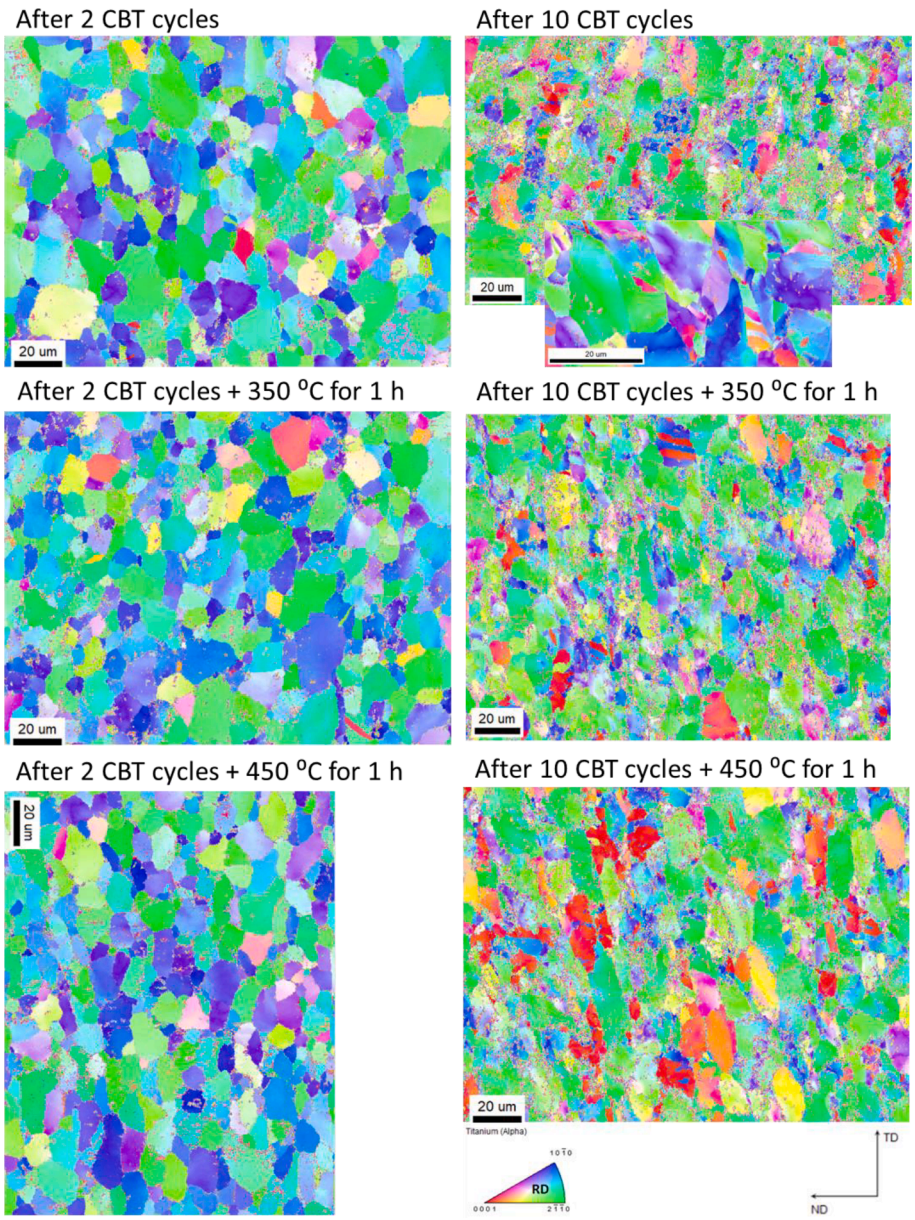

Fig. A6. IPF maps showing the evolution of grain structure during CBT along TD (at a pull speed of 1.35 mm/s and bending depth of 3.5) and annealing. The colors in the IPF triangle represent the orientation of the RD sheet axis relative to the frame of individual grains per map. The twins observed in the deformed structures are extension twins.

plasticity at the 2×/3× boundary, as revealed in Figs. 15 and 16. However, the developed localizations in CBT at the 2×/3× boundary are much smaller than necks developed during ST because the CBT process uniformly exhausts the great deal of ductility of the sheet. The localized regions become the ultimate fracture location exhibiting a very small neck. Tested samples experimentally fail at that location.

Furthermore, the simulation provided means to probe the axial stress and triaxiality through the sheet thickness to rationalize the role of thickness on ETF. As expected, the greatest tensile stress is the outer surface of the sheet undergoing CBT on the opposite side of rollers. Fig. 17 shows the stress underneath the middle roller. The magnitude increases with CBT cycled due to material hardening, while the shape of the profile is approximately constant. The two other rollers induce similar stress but of the opposite sign. Evidently, the combined bending and tension induce a non-symmetric tension/compression stress/strain profile with the neutral axis cyclically shifting to sheet surfaces opposite of the roller over which the sheet is going over. The magnitude of stress is a function of sheet thickness. Thicker sheets have greater stress for a fixed amount of bending depth. Moreover, thicker sheets have a greater portion of the stabilizing mechanism, which is the compressive portion of the stress/strain profile. The portion also have a favorable stress triaxiality. In contrast, thinner sheets can have the neutral axis leave the sheet thickness causing the entire sheet to be in tension. If this happens, the stabilizing mechanism vanishes causing the sheet to fail sooner. Hence, there is an optimal sheet thickness to go along with the CBT process parameters. Sheet experiences thinning during the process causing the profiles to evolve shifting the neutral axis, as the figure shows. Fig. 8 shows that 3.5 mm bending depth is optimal for 1 mm sheets of cp-Ti but it is around 3 mm for 2 mm sheets of cp-Ti. Fig. 17 also shows stress and triaxiality in the gauge section of the specimen away from the rollers. The nonsymmetric stress state in the specimens developed during CBT is such that it causes the specimens to bend permanently after releasing it from the machine (Barrett and Knezevic, 2020).

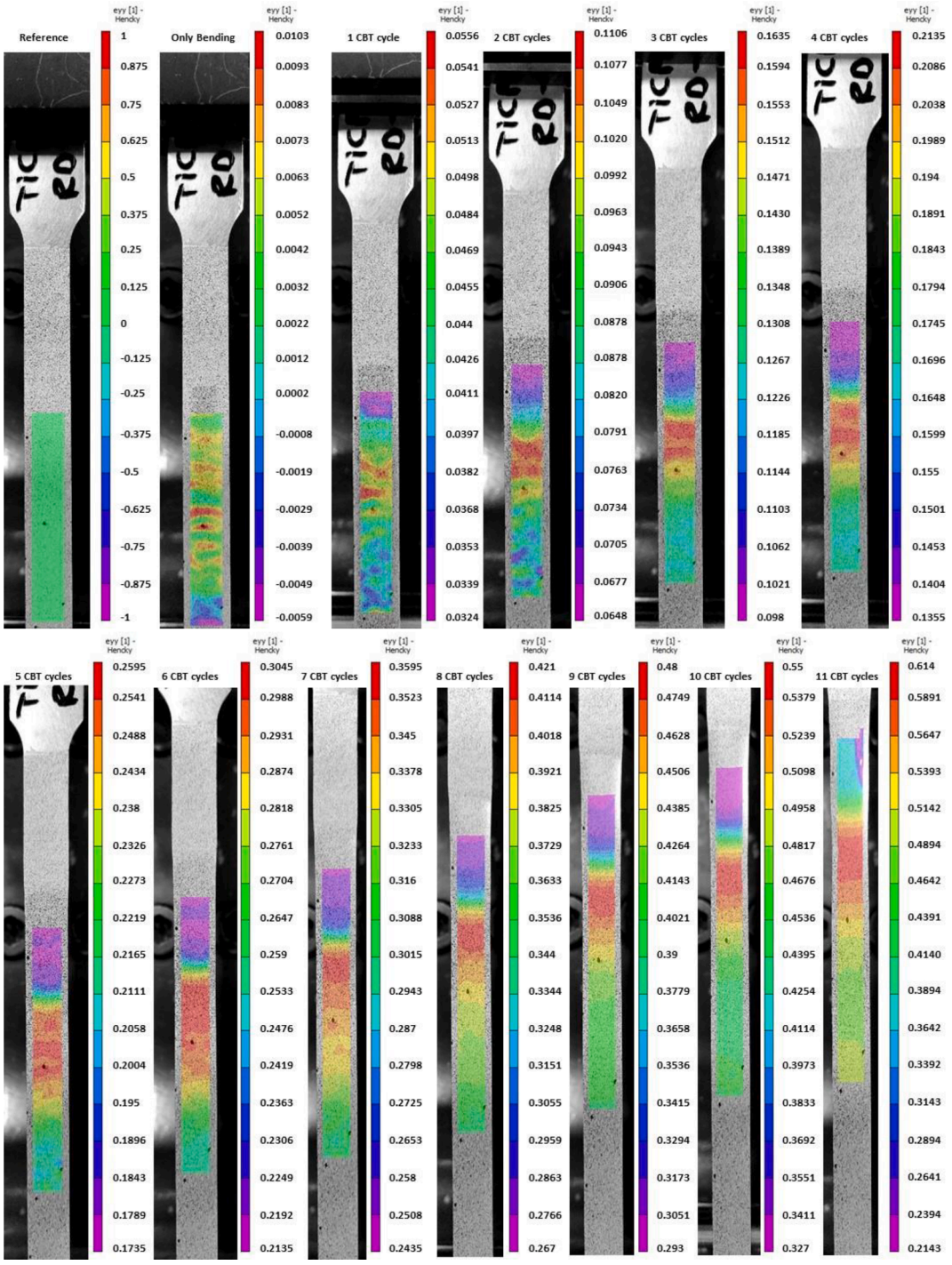

Fig. A7. A sequence of photographs and the corresponding strain fields measured by DIC during CBT testing to 11 cycles of a 1 mm thickness cp-Ti sheet (grade 4) along the RD.

5. Summary and conclusions

The present investigations allowed us to draw the following main conclusions:

- Load-displacement curves recoded along the RD, 45°, and TD during CBT of cp-Ti sheets were strong functions of applied crosshead velocity and bending depth process parameters, in addition to sheet thicknesses. A parametric study performed to establish a set of optimal parameters for enhancing ETF of cp-Ti under CBT revealed that ETF of the material can be enhanced with increasing the crosshead velocity and with increasing the bending depth up to a certain level, after which the ETF begins to decline. A detailed analysis of the data yielded 1.35 mm/s for crosshead velocity, 3.5 for bending depth, and 1.0 mm for sheet thickness as optimal. Under these optimized conditions, enhancements in ETF of about 2.9× to 3.5× were achieved using CBT relative to ST depending on the selected test direction.
- Testing the sheets of variable thickness revealed that ETF of the material can improve by selecting optimal sheet thickness. To this end, a reduction of the sheet thickness to 1.0 mm busted ETF relative to the 1.3 mm and 2 mm sheets. These finding were rationalized in

terms of the axial stress levels and stabilizing compressive stress both increasing with the sheet thickness under a given set of process parameters. The former negative and the latter positive effect of the CBT mechanics balance out at 1.0 mm thickness.

- Given the uniform elongation facilitated by CBT to strains much larger than uniform in ST, tradeoffs in strength and ductility of the material were examined by subjecting a set of sheet specimens to a certain number of CBT cycles under the optimized parameters and annealing. Strength of the material was found to increase by a factor of 1.3 along the sheet strongest direction, while by a factor of 1.6 along the sheet softest direction with 10 CBT cycles reducing the anisotropy. The significant improvements in strength originate from dislocations due to cold work. Given some grain refinement and change in grain morphology along with minor content of twinning in the structure after CBT, the strength increase must be owing to the increase in dislocation density. Ductility of $\sim$ 5% could be restored by annealing the material at 350 °C for one hour, while preserving a nearly isotropic material behavior.
- Pre-straining the material by CBT to variable strain levels, necessarily those greater than the necking strain level in ST, followed by secondary testing of the pre-strained sheets facilitated the identification of the post-necking hardening behavior of cp-Ti sheet metal for the first time. The stress–strain curves from the secondary ST tests were appropriately shifted for the level of strain accumulated during pre-straining by CBT for delineating the large strain flow curve.
- Relying on the extrapolated stress–strain curve, an FE simulation of the CBT process was performed to predict load–displacement as well as the stress and strain fields developing during the process. A finite element model of the process was created in Abaqus to simulate the CBT test while predicting the load–displacement data. Specifically, the model predicted the succession of spikes and plateaus inherent to the CBT load versus displacement curve verifying the extrapolated stress–strain curve.
- The simulation also provided means to probe the axial stress and triaxiality through the sheet thickness to rationalize the role of thickness on ETF. Moreover, strain localizations between 2 $\times$ and 3 $\times$ deformation regions were predicted and verified using the DIC measurements. However, the developed localizations in CBT were much smaller than necks developed during ST because the CBT process could uniformly exhaust the great deal of ductility of the sheet. The localized regions turn out to be the ultimate fracture location exhibiting a very small neck.
- The evolution of grain structure measured using EBSD revealed elongated grains in the pulling direction with substantial orientation spreads and some grain fragmentation because of severe straining during CBT. The scans showed minor activity of extension twinning. The structure was recovered by annealing. Measurements of texture evolution using NeD after ST and CBT showed similar features in pole figures with slightly higher intensities after CBT than ST because of the higher strain levels after CBT than ST. The characterization data revealed slip dominated deformation with a small twinning volume fraction. While some heterogeneous deformation could be attributed to the grain fragmentation and some twinning activity, the significant improvements in strength originate from dislocations and their structures.

Declaration of Competing Interest

The authors declare that they have no known competing financial interests or personal relationships that could have appeared to influence the work reported in this paper.

Data availability

Data will be made available on request.

Acknowledgments

This work is based upon projects supported by the U.S. National Science Foundation under a CAREER grant CMMI-1650641 and a GOALI grant CMMI-2147122.

Data availability

The raw/processed data required to reproduce these findings cannot be shared at this time due to technical or time limitations.

Appendix A

This appendix presents a table of basic properties based on the measured flow curves in Fig. 10 (Table A1). Moreover, Fig. A1 is a photograph of the CBT tester. Fig. A2 shows more data used to determine the optimum process parameters. Fig. A3 shows measured force–displacement curves during pre-straining of the CBT specimens. Fig. A4 shows more data used to determine heat treatment (HT) temperatures for pre-deformed specimens of cp-Ti. Fig. A5 shows KAM maps based on the maps from Fig. 11 and Fig. A6 shows additional IPF maps showing the evolution of grain structure during CBT along TD. Finally, Fig. A7 provides more DIC images.

References

ABAQUS Version 6, 2017. Dassault Systèmes, Providence, RI, USA.
Allwood, J.M., Shouler, D.R., 2009. Generalised forming limit diagrams showing increased forming limits with non-planar stress states. Int. J. Plast. 25 (7), 1207–1230.
ASTM E8/E8M-15a, 2015. Standard Test Methods for Tension Testing of Metallic Materials. ASTM International, West Conshohocken, PA.
Bachmann, F., Hielscher, R., Schaeben, H., 2010. Texture analysis with MTEX–free and open source software toolbox. Solid State Phenom. 160, 63–68.
Baral, M., Hama, T., Knudsen, E., Korkolis, Y.P., 2018. Plastic deformation of commercially-pure titanium: experiments and modeling. Int. J. Plast. 105, 164–194.
Barlat, F., Glazov, M., Brem, J., Lege, D., 2002. A simple model for dislocation behavior, strain and strain rate hardening evolution in deforming aluminum alloys. Int. J. Plast. 18, 919–939.
Barrett, T.J., Knezevic, M., 2019. Deep drawing simulations using the finite element method embedding a multi-level crystal plasticity constitutive law: experimental verification and sensitivity analysis. Comput. Methods Appl. Mech. Eng. 354, 245–270.
Barrett, T.J., Knezevic, M., 2020. Modeling material behavior during continuous bending under tension for inferring the post-necking strain hardening response of ductile sheet metals: application to DP 780 steel. Int. J. Mech. Sci. 174, 105508.
Barrett, T.J., Takagi, S., Islam, N., Kuwabara, T., Hassan, T., Kinsey, B.L., Knezevic, M., Korkolis, Y.P., 2021. Material modeling and simulation of continuous-bending-under-tension of AA6022-T4. J. Mater. Process. Technol. 287, 116658.
Bauschinger, J., 1886. Über die Veränderung der Elasticitätsgrenze und Festigkeit des Eisen und Stahls durch Strecken und Quetschen, durch Erwarmen und Abkühlen und durch oftmal wiederholte Beanspruchung. Mitteilungen aus dem mechanisch-technischen Laboratorium der k. polytechnischen Schule, 1877-1836.
Becker, H., Pantleon, W., 2013. Work-hardening stages and deformation mechanism maps during tensile deformation of commercially pure titanium. Comput. Mater. Sci. 76, 52–59.
Benedyk, J., Parikh, N., Stawarz, D., 1971. A method for increasing elongation values for ferrous and nonferrous sheet metals. J. Mater. 6, 16–29.
Bhattacharyya, A., Knezevic, M., Abouaf, M., 2015. Characterization of crystallographic texture and intra-grain morphology in cross-rolled tantalum. Metall. Mater. Trans. A 46 (3), 1085–1096.
Boyer, R.R., 1996. An overview on the use of titanium in the aerospace industry. Mater. Sci. Eng. A 213 (1-2), 103–114.
Coppieters, S., Kuwabara, T., 2014. Identification of post-necking hardening phenomena in ductile sheet metal. Exp. Mech. 54 (8), 1355–1371.
Daroju, S., Kuwabara, T., Knezevic, M., 2022. Experimental characterization and crystal plasticity modeling of dual-phase steels subjected to strain path reversals. Mech. Mater. 168, 104293.
Daroju, S., Kuwabara, T., Sharma, R., Fullwood, D.T., Miles, M.P., Knezevic, M., 2022. Experimental characterization and crystal plasticity modeling for predicting load reversals in AA6016-T4 and AA7021-T79. Int. J. Plast. 153, 103292.
Emmens, W.C., Boogaard, A.H.v.d., 2011. Cyclic stretch-bending: mechanics, stability and formability. J. Mater. Proc. Technol. 211, 1965–1981.
Emmens, W.C., van den Boogaard, A.H., 2009. An overview of stabilizing deformation mechanisms in incremental sheet forming. J. Mater. Process. Technol. 209 (8), 3688–3695.

Emmens, W.C., van den Boogaard, A.H., 2009. Incremental forming by continuous bending under tension—an experimental investigation. J. Mater. Process. Technol. 209 (14), 5456–5463.
Emmens, W.C., van den Boogaard, A.H., 2012. Material characterization at high strain by adapted tensile tests. Exp. Mech. 52 (8), 1195–1209.
Eyckens, P., Van Bael, A., Van Houtte, P., 2009. Marciniak-Kuczynski type modelling of the effect of through-thickness shear on the forming limits of sheet metal. Int. J. Plast. 25 (12), 2249–2268.
Ferreri, N.C., Savage, D.J., Knezevic, M., 2020. Non-acid, alcohol-based electropolishing enables high-quality electron backscatter diffraction characterization of titanium and its alloys: application to pure Ti and Ti-6Al-4V. Mater. Charact. 166, 110406.
Ferreri, N.C., Feng, Z., Savage, D.J., Brown, D.W., Clausen, B., Sisneros, T.A., Knezevic, M., 2022. In-situ high-energy X-ray diffraction and crystal plasticity modeling to predict the evolution of texture, twinning, lattice strains and strength during loading and reloading of beryllium. Int. J. Plast. 150, 103217.
Filice, L., Gagliardi, F., Lazzaro, S., Rocco, C., 2010. FE simulation and experimental considerations on TI alloy superplastic forming for aerospace applications. Int. J. Mater. Form. 3 (1), 41–46.
Hama, T., Nagao, H., Kobuki, A., Fujimoto, H., Takuda, H., 2015. Work-hardening and twinning behaviors in a commercially pure titanium sheet under various loading paths. Mater. Sci. Eng. A 620, 390–398.
Hariharan, K., Majidi, O., Kim, C., Lee, M., Barlat, F., 2013. Stress relaxation and its effect on tensile deformation of steels. Mater. Des. 1980–2015 (52), 284–288.
Hariharan, K., Dubey, P., Jain, J., 2016. Time dependent ductility improvement of stainless steel SS 316 using stress relaxation. Mater. Sci. Eng. A 673, 250–256.
Hosford, W.F., Caddell, R.M., 2011. Metal forming: mechanics and metallurgy. Cambridge University Press, New York, USA.
Knezevic, M., Kalidindi, S.R., 2007. Fast computation of first-order elastic-plastic closures for polycrystalline cubic-orthorhombic microstructures. Comput. Mater. Sci. 39 (3), 643–648.
Knezevic, M., Kalidindi, S.R., Mishra, R.K., 2008. Delineation of first-order closures for plastic properties requiring explicit consideration of strain hardening and crystallographic texture evolution. Int. J. Plast. 24 (2), 327–342.
Knezevic, M., Levinson, A., Harris, R., Mishra, R.K., Doherty, R.D., Kalidindi, S.R., 2010. Deformation twinning in AZ31: Influence on strain hardening and texture evolution. Acta. Mater. 58 (19), 6230–6242.
Knezevic, M., Lebensohn, R.A., Cazacu, O., Revil-Baudard, B., Proust, G., Vogel, S.C., Nixon, M.E., 2013. Modeling bending of α-titanium with embedded polycrystal plasticity in implicit finite elements. Mater. Sci. Eng. A 564, 116–126.
Knezevic, M., Zecevic, M., Beyerlein, I.J., Bingert, J.F., McCabe, R.J., 2015. Strain rate and temperature effects on the selection of primary and secondary slip and twinning systems in HCP Zr. Acta Mater. 88, 55–73.
Knezevic, M., Crapps, J., Beyerlein, I.J., Coughlin, D.R., Clarke, K.D., McCabe, R.J., 2016. Anisotropic modeling of structural components using embedded crystal plasticity constructive laws within finite elements. Int. J. Mech. Sci. 105, 227–238.
Knezevic, M., Poulin, C.M., Zheng, X., Zheng, S., Beyerlein, I.J., 2019. Strengthening of alloy AA6022-T4 by continuous bending under tension. Mater. Sci. Eng. A 758, 47–55.
Knezevic, M., Ghorbanpour, S., Ferreri, N.C., Riyad, I.A., Kudzal, A.D., Paramore, J.D., Vogel, S.C., McWilliams, B.A., 2021. Thermo-hydrogen refinement of microstructure to improve mechanical properties of Ti–6Al–4V fabricated via laser powder bed fusion. Mater. Sci. Eng. A 809, 140980.
Lee, M.-S., Hyun, Y.-T., Jun, T.-S., 2019. Global and local strain rate sensitivity of commercially pure titanium. J. Alloys Compd. 803, 711–720.
Luan, Q., Britton, T.B., Jun, T.-S., 2018. Strain rate sensitivity in commercial pure titanium: the competition between slip and deformation twinning. Mater. Sci. Eng. A 734, 385–397.
Manopulo, N., Raemy, C., Hora, P., 2018. A flexible modelling approach for capturing plastic anisotropy and strength differential effects exhibited by commercially pure titanium. Int. J. Solids Struct. 151, 91–98.
Matukhno, N., Kljestan, N., Vogel, S.C., Knezevic, M., 2022. Cyclic bending under tension of alloy AZ31 sheets: influence on elongation-to-fracture and strength. Mater. Sci. Eng. A 857, 144127.
Nasiri-Abarbekoh, H., Ekrami, A., Ziaei-Moayyed, A.A., Shohani, M., 2012. Effects of rolling reduction on mechanical properties anisotropy of commercially pure titanium. Mater. Des. 34, 268–274.
Nine, H.D., 1979. Drawbead forces in sheet metal forming. In: Koistinen, D.P., Wang, N.-M. (Eds.), Mechanics of Sheet Metal Forming. Springer US, Boston, MA, pp. 179–211.
Peng, J., Zhou, C.-Y., Dai, Q., He, X.-H., 2013. An improved constitutive description of tensile behavior for CP-Ti at ambient and intermediate temperatures. Mater. Des. 50, 968–976.
Poulin, C.M., Korkolis, Y.P., Kinsey, B.L., Knezevic, M., 2019. Over five-times improved elongation-to-fracture of dual-phase 1180 steel by continuous-bending-under-tension. Mater. Des. 161, 95–105.
Poulin, C.M., Barrett, T.J., Knezevic, M., 2020. Inferring post-necking strain hardening behavior of sheets by a combination of continuous bending under tension testing and finite element modeling. Exp. Mech. 60 (4), 459–473.
Poulin, C.M., Vogel, S.C., Korkolis, Y.P., Kinsey, B.L., Knezevic, M., 2020. Experimental studies into the role of cyclic bending during stretching of dual-phase steel sheets. Int. J. Mater. Form. 13 (3), 393–408.
Revil-Baudard, B., Cazacu, O., Massoni, E., 2021. Room-temperature plastic behavior and formability of a commercially pure titanium: Mechanical characterization, modeling, and validation. Int. J. Solids Struct. 228, 111121.
Risse, M., Lentz, M., Fahrenson, C., Reimers, W., Knezevic, M., Beyerlein, I.J., 2017. Elevated temperature effects on the plastic anisotropy of an extruded Mg-4 Wt Pct Li alloy: experiments and polycrystal modeling. Metall. Mater. Trans. A 48 (1), 446–458.
Riyad, I.A., Feather, W.G., Vasilev, E., Lebensohn, R.A., McWilliams, B.A., Pilchak, A.L., Knezevic, M., 2021. Modeling the role of local crystallographic correlations in microstructures of Ti-6Al-4V using a correlated structure visco-plastic self-consistent polycrystal plasticity formulation. Acta Mater. 203, 116502.
Riyad, I.A., McWilliams, B.A., Pramanik, B., Knezevic, M., 2023. Correlated structure viscoplastic self-consistent polycrystal plasticity: application to modeling strain rate sensitive deformation of Ti-6Al-4 V. Int. J. Plast. 163, 103571.
Roemer, T.J., Barrett, T.J., Knezevic, M., Kinsey, B.L., Korkolis, Y.P., 2019. Experimental study of continuous-bending-under-tension of AA6022-T4. J. Mater. Process. Technol. 266, 707–714.
Savage, D.J., McCabe, R.J., Knezevic, M., 2021. An automated procedure built on MTEX for reconstructing deformation twin hierarchies from electron backscattered diffraction datasets of heavily twinned microstructures. Mater. Charact. 171, 110808.
Savage, D.J., Feng, Z., Knezevic, M., 2021. Identification of crystal plasticity model parameters by multi-objective optimization integrating microstructural evolution and mechanical data. Comput. Methods Appl. Mech. Eng. 379, 113747.
Schleich, R., Held, C., Sindel, M., Liewald, M., 2009. Investigation on the effect of curvature and sheet thickness on forming limit prediction for aluminium sheet metal alloys. Int. J. Mater. Form. 2 (S1), 411–414.
Sharma, R., Sargeant, D., Daroju, S., Knezevic, M., Miles, M.P., Fullwood, D.T., 2022. Multi-strain path deformation behavior of AA6016-T4: experiments and crystal plasticity modeling. Int. J. Solids Struct. 244-245, 111536.
Sinha, S., Gurao, N.P., 2017. In situ electron backscatter diffraction study of twinning in commercially pure titanium during tension-compression deformation and annealing. Mater. Des. 116, 686–693.
Staiger, M.P., Pietak, A.M., Huadmai, J., Dias, G., 2006. Magnesium and its alloys as orthopedic biomaterials: a review. Biomaterials 27 (9), 1728–1734.
Swift, H., 1948. Plastic bending under tension. Engineering 166, 333–359.
Tamimi, S., Sivaswamy, G., Siddiq, M.A., Rahimi, S., Leacock, A., Blackwell, P., 2020. Mechanical response and microstructure evolution of commercially pure titanium subjected to repetitive bending under tension. Mater. Des. 193, 108814.
Tsao, L.C., Wu, H.Y., Leong, J.C., Fang, C.J., 2012. Flow stress behavior of commercial pure titanium sheet during warm tensile deformation. Mater. Des. 34, 179–184.
Varma, A., Gokhale, A., Jain, J., Hariharan, K., Cizek, P., Barnett, M., 2018. Investigation of stress relaxation mechanisms for ductility improvement in SS316L. Phil. Mag. 98 (3), 165–181.
Wang, Y., He, W., Liu, N., Chapuis, A., Luan, B., Liu, Q., 2018. Effect of pre-annealing deformation on the recrystallized texture and grain boundary misorientation in commercial pure titanium. Mater. Charact. 136, 1–11.
Wang, J., Zecevic, M., Knezevic, M., Beyerlein, I.J., 2020. Polycrystal plasticity modeling for load reversals in commercially pure titanium. Int. J. Plast. 125, 294–313.
Wang, J., Zhu, G., Wang, L., Vasilev, E., Park, J.-S., Sha, G., Zeng, X., Knezevic, M., 2021. Origins of high ductility exhibited by an extruded magnesium alloy Mg-1.8Zn-0.2Ca: experiments and crystal plasticity modeling. J. Mater. Sci. Technol. 84, 27–42.
Wenk, H.-R., Lutterotti, L., Vogel, S., 2003. Texture analysis with the new HIPPO TOF diffractometer. Nucl. Instrum. Methods Phys. Res., Sect. A 515 (3), 575–588.
Wenk, H.-R., Lutterotti, L., Vogel, S.C., 2010. Rietveld texture analysis from TOF neutron diffraction data. Powder Diffr. 25 (3), 283–296.
Wu, X., Proust, G., Knezevic, M., Kalidindi, S.R., 2007. Elastic-plastic property closures for hexagonal close-packed polycrystalline metals using first-order bounding theories. Acta. Mater. 55 (8), 2729–2737.
Yaddanapudi, K., Knezevic, M., Mahajan, S., Beyerlein, I.J., 2021. Plasticity and structure evolution of ferrite and martensite in DP 1180 during tension and cyclic bending under tension to large strains. Mater. Sci. Eng. A 820, 141536.
Yagami, T., Manabe, K., Miyamoto, T., 2009. Ductile fracture behavior of 5052 aluminum alloy sheet under cyclic plastic deformation at room temperature. J. Mater. Process. Technol. 209 (2), 1042–1047.
Zecevic, M., Knezevic, M., 2015. A dislocation density based elasto-plastic self-consistent model for the prediction of cyclic deformation: Application to Al6022-T4. Int. J. Plast. 72, 200–217.
Zecevic, M., Knezevic, M., 2017. Modeling of sheet metal forming based on implicit embedding of the elasto-plastic self-consistent formulation in shell elements: application to cup drawing of AA6022-T4. JOM 69 (5), 922–929.
Zecevic, M., Knezevic, M., 2018. Latent hardening within the elasto-plastic self-consistent polycrystal homogenization to enable the prediction of anisotropy of AA6022-T4 sheets. Int. J. Plast. 105, 141–163.
Zecevic, M., Knezevic, M., 2023. Origins of improved elongation to fracture in cyclic bending under tension of AA6022-T4 sheets as revealed using crystal plasticity modeling. Mech. Mater. 177, 104546.
Zecevic, M., Korkolis, Y.P., Kuwabara, T., Knezevic, M., 2016. Dual-phase steel sheets under cyclic tension–compression to large strains: experiments and crystal plasticity modeling. J. Mech. Phys. Solids 96, 65–87.
Zecevic, M., Roemer, T., Knezevic, M., Korkolis, Y., Kinsey, B., 2016. Residual ductility and microstructural evolution in continuous-bending-under-tension of AA-6022-T4. Materials 9, 130.
Zecevic, M., Knezevic, M., Beyerlein, I.J., McCabe, R.J., 2016. Texture formation in orthorhombic alpha-uranium under simple compression and rolling to high strains. J. Nucl. Mater. 473, 143–156.
Zecevic, M., Pantleon, W., Lebensohn, R.A., McCabe, R.J., Knezevic, M., 2017. Predicting intragranular misorientation distributions in polycrystalline metals using the viscoplastic self-consistent formulation. Acta Mater. 140, 398–410.

Zecevic, M., Beyerlein, I.J., Knezevic, M., 2017. Coupling elasto-plastic self-consistent crystal plasticity and implicit finite elements: applications to compression, cyclic tension-compression, and bending to large strains. Int. J. Plast. 93, 187–211.
Zecevic, M., Beyerlein, I.J., Knezevic, M., 2018. Activity of pyramidal I and II <c+a> slip in Mg alloys as revealed by texture development. J. Mech. Phys. Solids 111, 290–307.
Zecevic, M., Lebensohn, R.A., Rogers, M., Moore, J., Chiravalle, V., Lieberman, E., Dunning, D., Shipman, G., Knezevic, M., Morgan, N., 2021. Viscoplastic self-consistent formulation as generalized material model for solid mechanics applications. Applications Eng. Sci. 6, 100040.
Zhai, J., Luo, T., Gao, X., Graham, S.M., Baral, M., Korkolis, Y.P., Knudsen, E., 2016. Modeling the ductile damage process in commercially pure titanium. Int. J. Solids Struct. 91, 26–45.
Zhu, X.J., Tan, M.J., Zhou, W., 2005. Enhanced superplasticity in commercially pure titanium alloy. Scr. Mater. 52 (7), 651–655.